NJC

PAPER

View Article Online
View Journal

Open Access Article. Published on 08 April 2026. Downloaded on 4/8/2026 8:29:56 PM.
This article is licensed under a Creative Commons Attribution-NonCommercial 3.0 Unported Licence.

Check for updates

Cite this: DOI: 10.1039/d5nj04998a

Visible-light-driven Co–Al LDH/g-C_3N_5 nanoarchitecture for dual pollutant degradation and sustainable H_2O_2 production with photoluminescence detection capability

Alaka Rath,[a] Pratyush Kumar Sahu,[a] Vibhav Shukla,[b] Aslisha Champati,[a] Kafeel Ahmad Siddiqui[b] and Brundabana Naik*[a]

Received 29th December 2025,
Accepted 7th March 2026

DOI: 10.1039/d5nj04998a

rsc.li/njc

The development of efficient and sustainable photocatalysts for environmental remediation is of significant interest in addressing the rising concerns of pharmaceutical and dye contaminants in aquatic systems. In this work, a Co–Al layered double hydroxide (Co–Al LDH) decorated on a nitrogen-enriched graphitic carbon nitride (g-C_3N_5) nanocomposite (LN) with varying weight ratios (1 : 2, 1 : 1, 2 : 1) was successfully synthesised *via* a facile solvothermal method followed by ultrasonic exfoliation. The optimised LN2 : 1 catalyst with enhanced photocatalytic behaviour was evaluated for photocatalytic organic pollutant degradation, oxygen reduction reaction (ORR) and antibiotic detection *via* photoluminescence sensing. The LN2 : 1 nanocomposite achieved the highest degradation efficiency of 93.4% against ciprofloxacin (CIP) and 92.1% against Cresol Red (CR) within 120 minutes under solar irradiation, demonstrating its superior catalytic activity compared to pristine g-C_3N_5 and Co–Al LDH. Furthermore, the composite demonstrated enhanced hydrogen peroxide (H_2O_2) generation of 1903.28 $\mu M\ L^{-1}$ (5.5 times that of g-C_3N_5 and 16.43 times that of Co–Al LDH), which was substantially higher than that of pristine components, indicating its ability to drive reactive oxygen species (ROS)-mediated photocatalytic pathways. Moreover, LN2 : 1 showed the most efficient photoluminescence sensing performance toward ciprofloxacin (CIP), achieving a limit of detection (LOD) of 0.982 ppm and R^2 of 0.979. The BET surface area analysis demonstrated a 2D nano-platelet-like composite with a higher surface area of 30.647 $m^2\ g^{-1}$, indicative of a structure with abundant active sites for light harvesting and catalytic activation. Experimental analysis, including electrochemical analysis and radical scavenging tests, indicated the involvement of a Type-II mechanism, which markedly enhances charge carrier separation and utilisation, facilitating the generation of ROS such as superoxide ($^\bullet O_2^-$) and hydroxyl ($^\bullet OH$) radicals that drive REDOX processes. This study provides a sustainable photocatalytic strategy with the potential to tackle real-world environmental challenges by enabling efficient degradation of emerging contaminants and advancing water purification technologies.

1. Introduction

The intensifying global crisis of environmental pollution constitutes a formidable threat to planetary health, human well-being, and sustainable development. Wastewater from pharmaceuticals and dyes often comprises a wide range of chemicals and compounds.[1] While pharmaceutical industry effluents may contain organic solvents, pharmaceutical residues, and other pollutants, dye industry effluents usually contain trace levels of dyes, solvents, and heavy metals.[2] Anthropogenic activities such as rapid industrialisation, urban expansion, and increased consumption of synthetic chemicals have led to the pervasive emission of hazardous pollutants into the air, water, and soil, surpassing the planet's natural assimilative and regenerative capacities.[3] Airborne contaminants, particularly particulate matter and persistent organic pollutants, are implicated in approximately 8 million premature deaths annually, as well as acute respiratory and cardiovascular disorders.[4] Chemical pollutants, including pharmaceutical residues and industrial dyes, represent a growing concern, with recent evidence highlighting their bioaccumulation and biomagnification across trophic levels, ultimately undermining ecosystem integrity and endangering biodiversity.[5] In response

---

[a] *Department of Chemistry, ITER, Siksha O' Anusandhan, deemed to be University, Bhubaneshwar, Odisha, India. E-mail: brundabananaik@soa.ac.in*

[b] *Department of Chemistry, National Institute of Technology Raipur, G E Road, Raipur, 492010, Chhattisgarh, India*

Open Access Article. Published on 08 April 2026. Downloaded on 4/8/2026 8:29:56 PM.
This article is licensed under a Creative Commons Attribution-NonCommercial 3.0 Unported Licence.

to this escalating crisis, international frameworks such as the Global Framework on Chemicals and multilateral environmental treaties have advocated for stringent emission controls and comprehensive pollutant management.[6,7] Notably, the progressive transition towards a circular economy, the implementation of advanced waste treatment infrastructures, and the recalcitrance of many synthetic organic contaminants, such as drugs and dyes, remain critical remediation challenges, as conventional treatment technologies are often inadequate for their complete mineralisation.[8] Against this backdrop, heterogeneous photocatalysis has emerged as a paradigm-shifting technology for environmental remediation, particularly in the abatement of recalcitrant organic pollutants.[9] Due to its potential to address environmental issues, semiconductor photocatalysis has garnered attention in the past few years.[10] Recent investigations have demonstrated that engineered photocatalysts such as graphitic carbon nitride-based nanocomposites, metal-doped layered double hydroxides, and Z-scheme heterojunctions exhibit remarkable efficacy in facilitating the oxidative degradation of a broad spectrum of pharmaceutical compounds and synthetic dyes under visible light irradiation.[11,12] For instance, bespoke nanomaterials are capable of achieving degradation efficiencies exceeding 90% for complex dye molecules like methylene blue, rhodamine B, Cresol Red, and pharmaceuticals within a few hours of photoreaction.[13,14] The advanced oxidation processes involved in photocatalysis not only mineralise the parent compounds but also mitigate the formation of toxic intermediates, thereby offering a sustainable and energy-efficient approach to pollutant abatement.[15] Specifically, ciprofloxacin (CIP), a broad-spectrum fluoroquinolone antibiotic, has emerged as a pervasive environmental contaminant of major exotoxicological concern due to its extensive use in both human and veterinary medicine.[16] Globally, relentless consumption and improper disposal pathways encompassing pharmaceutical manufacturing effluents, hospital and agricultural run-off, and incomplete removal during conventional wastewater treatment have resulted in significant and widespread dissemination of CIP residues into diverse environmental matrices, including surface water, sediments, and soils.[17,18] It is estimated that between 40 and 90% of administered antibiotics may be excreted unmetabolized, enabling substantial environmental release.[19] The environmental fallout of CIP includes inhibition of key microbial and nutrient cycling functions, phytotoxicity, and the accelerated emergence and dissemination of antimicrobial resistance genes, posing significant risks to both ecological and public health.[20] These trends underscore the urgent imperative for advanced remediation technologies and robust regulatory frameworks to restrain CIP's environmental dissemination and protect ecosystem integrity.[21] To solve this hazardous quest, photocatalysis stands at the forefront of contemporary environmental remediation strategies, offering a transformative solution to the multifaceted challenges posed by residual ciprofloxacin in ecological compartments.[22–24] The persistent recalcitrance and bioaccumulative tendencies of CIP not only catalyse adverse effects but also escalate the spread of antimicrobial resistance genes across trophic levels.[18,25] Conventional treatment modalities have proved largely inadequate, typically failing to achieve complete mineralisation or to avert the generation of secondary toxic byproducts.[26,27] In this context, heterogeneous photocatalysis provides a robust, sustainable and high-efficiency paradigm by harnessing advanced semiconductor materials such as TiO_2,[22] g-C_3N_4,[28] and doped LDH composites to catalyse the oxidative degradation of CIP under solar or artificial light irradiation.[29] The underlying process is predicated on the photogeneration of electron–hole pairs, which initiate a cascade of advanced oxidation reactions yielding highly reactive radical species ($^{\bullet}OH$, $O_2^{\bullet-}$) capable of cleaving the complex molecular scaffold of CIP and its resistant metabolites.[30] Recent investigations highlight that optimised photocatalytic systems can achieve ∼70–90% degradation of CIP within hours, with kinetic analyses often adhering to pseudo-first order reaction models and demonstrating recyclability, low energy penalties, and superior environmental compatibility.[31] Through the efficient activation and reduction of molecular oxygen, photocatalytic systems employing ORR generate potent reactive oxygen species such as hydrogen peroxide (H_2O_2) and superoxide radicals ($O_2^{\bullet-}$) that can oxidatively dismantle the robust chemical architecture of antibiotics, dyes, and pharmaceutical residues with remarkable efficiencies.[32] This mechanism confers substantial advantages such as accelerated degradation kinetics, enhanced mineralisation to benign end-products, and diminished risks of byproduct toxicity and antimicrobial resistance propagation.[33,34] State-of-the-art organic and inorganic photocatalysts engineered for superior ORR performance leverage tailored bandgaps, abundant active sites, and optimal charge separation, ensuring selective, stable, and scalable pollutant remediation under ambient conditions.[35]

The oxygen reduction reaction (ORR), a central process in electrochemical energy systems, presents remarkable opportunities for sustainable chemical synthesis, particularly through its selective two-electron pathway for hydrogen peroxide (H_2O_2) generation.[36,37] Conventionally, industrial H_2O_2 production relies on the energy-intensive anthraquinone process, which requires complex catalysts, organic solvents, and transportation logistics that pose significant safety and environmental concerns.[38] In contrast, electrochemical H_2O_2 synthesis *via* the $2e^-$ ORR pathway offers a direct, green, and localised production route that employs only water, oxygen, and electricity as inputs.[39] This clean approach eliminates hazardous hydrogen–oxygen mixtures, operates under ambient conditions, and can be powered by renewable energy sources such as solar or wind, thereby achieving near-zero carbon emissions.[40,41] Mechanistically, the $2e^-$ ORR proceeds through the stepwise reduction of O_2 to the hydroperoxide ion (HO_2^-) or H_2O_2, depending on pH, with key intermediates like $^{\bullet}OOH$ determining selectivity and kinetics.[42] The reaction pathway competes with the conventional $4e^-$ ORR route leading to water formation, making catalyst design central to directing selectivity towards H_2O_2 production.[43] Advanced carbon-based, heteroatom-doped, and single-atom catalysts have shown promise in modulating the adsorption energies of intermediates and optimising the

Open Access Article. Published on 08 April 2026. Downloaded on 4/8/2026 8:29:56 PM.
This article is licensed under a Creative Commons Attribution-NonCommercial 3.0 Unported Licence.

reaction's thermodynamics and kinetics, while novel reactor configurations such as gas diffusion electrodes and flow cells enhance mass transfer and scalability.[44] From a broader perspective, H_2O_2 stands as a multifunctional oxidant and energy carrier critical to several environmental and industrial sectors. Its applications span advanced oxidation processes for wastewater treatment, antibacterial and sterilisation systems, chemical synthesis, paper and textile bleaching, and energy conversion technologies.[45] The ability to generate H_2O_2 electrocatalytically at the point of use not only reduces reliance on centralised infrastructure but also opens up pathways for integrated reaction systems, such as coupling with organic oxidation or CO_2 reduction, to produce high-value chemicals with improved overall energy efficiency.[46] Thus, the exploration of $2e^-$ ORR-driven H_2O_2 electrosynthesis represents a transformative direction in sustainable technology, bridging electrochemistry, materials science, and environmental engineering towards decentralised, circular, and carbon-neutral chemical production.[39,47]

Layered double hydroxides (LDHs), belonging to the family of two-dimensional (2D) materials, have attracted extensive research interest across multiple scientific disciplines, including catalysis, adsorption, and energy storage, owing to their distinctive structural and chemical characteristics.[48,49] These materials consist of positively charged brucite-like layers accompanied by charge-neutralising anions located in the interlayer region, providing a highly adaptable platform for tailoring their properties through compositional and structural tuning.[50] The general chemical representation of LDHs can be expressed as $[M_{1-x}^{2+}M_x^{3+}(OH)_2]^{x+}(A^{n-})_{x/n}\cdot mH_2O$, where M^{2+} and M^{3+} denote divalent and trivalent metal cations, respectively. A^{n-} corresponds to the interlayer anion and x represents the molar ratio of M^{3+} to $(M^{2+} + M^{3+})$.[50,51] The intrinsic layered architecture of LDHs results in a high surface area and adjustable interlayer spacing, enabling efficient diffusion of reactants to the active sites. Moreover, their capacity to accommodate various cations and anions within the framework allows for fine-tuning of functionalities.[52] This compositional flexibility is crucial for optimising the electronic structure and redox behaviour, both essential for catalytic reactions.[48] In photocatalysis, LDHs have emerged as highly promising candidates for environmental remediation and sustainable energy applications.[53] Their ability to absorb photons and generate electron–hole pairs, combined with their high surface area, makes them effective in degrading organic pollutants and producing renewable fuels.[54] Enhancements in photocatalytic efficiency can be achieved through several strategies, including heterostructure formation, defect engineering, and metal ion doping.[55] Constructing LDH-semiconductor heterojunctions is particularly advantageous, as coupling with semiconductors that possess compatible band structures enhances charge separation and transport, minimising recombination losses and improving photocatalytic response.[56] Furthermore, the synergistic effect between the LDH and the semiconductor components can lead to improved light absorption and increased active sites.[57] The introduction of defects, such as oxygen vacancies, into the LDH structure can also enhance photocatalytic activity by creating additional active sites and facilitating charge transfer.[58] Similarly, doping with metal ions can modify the electronic properties of LDHs, leading to improved light adsorption and enhanced redox activity.[59,60] The application of LDHs in photocatalysis spans a wide range of environmental and energy-related processes. They have been successfully employed for the degradation of various organic pollutants, including dyes, pharmaceuticals, and pesticides, from aqueous solutions.[61] Furthermore, LDHs have shown promise in photocatalytic water splitting for hydrogen production and CO_2 reduction for the synthesis of renewable fuels.[62] Their versatility and tunable properties make LDHs a valuable material platform for addressing pressing environmental and energy challenges through photocatalytic processes.[63]

2. Experimental section

2.1. Reagents

Cobalt nitrate hexahydrate (MERCK), aluminium nitrate nonahydrate (Sigma-Aldrich), sodium hydroxide pellets (MERCK), sodium carbonate (Sigma-Aldrich), nitric acid (MERCK), ciprofloxacin hydrochloride monohydrate (Sigma-Aldrich), 3-amino-1,2,4-triazole (Sigma-Aldrich), 2-propanol (MERCK), *p*-benzoquinone (MERCK), citric acid (MERCK), dimethyl sulfoxide (MERCK), methanol (SRL), absolute ethanol (SRL), chloroform (LOBA), tetrahydrofuran (Sigma-Aldrich), dimethylformamide (Sigma-Aldrich), acetonitrile (Sigma-Aldrich), nitrobenzene (MERCK), dichloromethane (Sigma-Aldrich), acetone (SRL), chloramphenicol (Sigma-Aldrich), roxithromycin (Sigma-Aldrich), naproxen (Sigma-Aldrich), nitrofurantoin (Sigma-Aldrich), norfloxacin (Sigma-Aldrich), metronidazole (Sigma-Aldrich), ofloxacin (Sigma-Aldrich), colchine (Sigma-Aldrich), riboflavon (Sigma-Aldrich), Aquivion (Sigma-Aldrich), and sodium sulphate (Sigma-Aldrich) were used. All the chemicals were of analytical grade and were used without further purification.

2.2. Synthesis of g-C_3N_5

The synthesis of g-C_3N_5 was carried out by thermal polymerisation, using 3-amino-1,2,4-triazole as the precursor. In the conventional method, 3-amino-1,2,4-triazole was calcined at 500 °C for a duration of three hours in a controlled air environment, applying a heating rate of 10 °C per minute. After cooling naturally to ambient temperature, the resulting g-C_3N_5 appeared as a brown solid. Subsequent exfoliation of this material was achieved by ultrasonication in water for three hours. The final product was then separated by centrifuging the suspension for 10 minutes, and dried overnight at 80 °C.[64]

2.3. Synthesis of Co–Al LDH

The synthesis of pure Co–Al LDH was performed using a simple co-precipitation method. Cobalt nitrate hexahydrate (0.125 M, 3.363 g) and aluminium nitrate nonahydrate (0.083 M, 0.124 g) were dissolved in 100 mL of deionised water to form the precursor solution. Separately, an alkaline mixture was prepared by dissolving 2.4 g of NaOH and 3.18 g of Na_2CO_3 in

Open Access Article. Published on 08 April 2026. Downloaded on 4/8/2026 8:29:56 PM.
This article is licensed under a Creative Commons Attribution-NonCommercial 3.0 Unported Licence.

water. This alkaline solution was steadily added dropwise under continuous stirring to the precursor solution, leading to the precipitation of LDH. Nitric acid was added dropwise to maintain the pH of the suspension at 7. The mixture was then stirred at 80 °C for 24 hours. After the reaction, the LDH precipitates were collected by vacuum filtration, washed thoroughly, and filtered again before drying at 80 °C for 12 hours, yielding a fine powder.[65]

2.4. Synthesis of Co–Al LDH/g-C_3N_5

The decoration of exfoliated 2D g-C_3N_5 nanosheets with 2D Co–Al LDH was achieved using a facile *in situ* hydrothermal method. Initially, for the synthesis of the LN1 : 1 composite, a specified quantity of 0.5 g of g-C_3N_5 was dispersed in 15 mL of deionised water by ultrasonication for 30 minutes at room temperature to obtain a uniform suspension. Subsequently, 0.436 g of cobalt nitrate hexahydrate and 0.195 g of aluminium nitrate nonahydrate were added in a 2 : 1 molar ratio, and the mixture was stirred for 30 minutes to promote thorough mixing. Dropwise addition of an aqueous NaOH solution followed, after which the mixture was transferred into a Teflon-lined stainless steel autoclave and subjected to hydrothermal treatment at 120 °C for 12 hours. The resulting product was washed with water and dried at 60 °C for 12 hours. Similarly, the other 2 composites were prepared following the same synthesis procedure. The composites formed were identified as LN1 : 1, LN1 : 2 and LN2 : 1 depending on the relative proportions used (Scheme 1).[66]

3. Experimental setup

3.1. Fluorescence sensing experiment

The luminescence characteristics of Co–Al LDH, LN2 : 1 and g-C_3N_5 were assessed in both aqueous and ethanol solutions at ambient temperature. Before measurement, the samples underwent an activation step involving immersion in pure methanol for 24 hours, followed by vacuum drying at 30 °C for another 24 hours. This activation is believed to improve surface accessibility and increase the density of active sites, thus enhancing the sensing capabilities of Co–Al LDH, LN2 : 1 and g-C_3N_5.

The fluorescence sensing ability of Co–Al LDH, LN2 : 1, and g-C_3N_5 was investigated through preliminary screening with different solvents and antibiotics. For fluorescence measurements, 4 mg of finely grounded Co–Al LDH, LN2 : 1, and g-C_3N_5 was dispersed in 5 mL of various solvents, including water (H_2O), chloroform ($CHCl_3$), tetrahydrofuran (THF), dimethylformamide (DMF), acetonitrile (CH_3CN), nitrobenzene (NB), ethanol (EtOH), methanol (MeOH), diethylformamide (DEF), dichloromethane (DCM), acetone, and isopropanol. The suspensions were subjected to 60 minutes of sonication and subsequently kept undisturbed for 24 hours to ensure stability. The emission spectra were collected at room temperature using an excitation wavelength of 300 nm, spanning the spectral range of 200 to 600 nm. The fluorescence intensity was observed for Co–Al LDH, LN2 : 1, and g-C_3N_5.[67–69]

To evaluate the potential of Co–Al LDH, LN2 : 1, and g-C_3N_5 as a fluorescence sensor for water-soluble antibiotics, 3 mg of

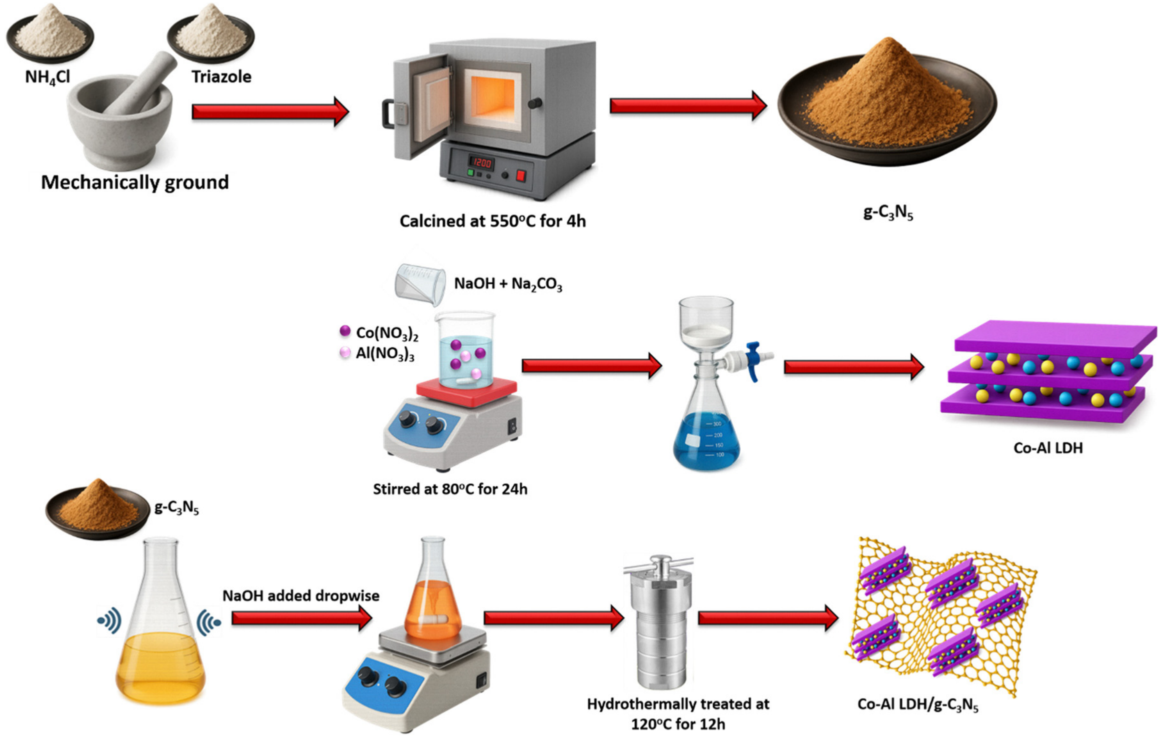

Scheme 1 Schematic illustration of the synthesis of g-C_3N_5, Co–Al LDH, and LN composites.

This journal is © The Royal Society of Chemistry and the Centre National de la Recherche Scientifique 2026

Open Access Article. Published on 08 April 2026. Downloaded on 4/8/2026 8:29:56 PM. This article is licensed under a Creative Commons Attribution-NonCommercial 3.0 Unported Licence.

the material was dispersed in 4 mL of aqueous, ethanol and aqueous-based solutions (for Co–Al LDH, LN2 : 1, and g-C_3N_5 respectively) containing commonly used antibiotics, namely chloramphenicol (CAP), roxithromycin (RXM), naproxen (NPX), nitrofurantoin (NFT), norfloxacin (NFX), ciprofloxacin (CIP), metronidazole (MTZ), ofloxacin (OFL), colchicine (COL), and riboflavin (RBF). The luminescence spectra of the resulting suspensions were recorded after 30 minutes of sonication. Furthermore, aqueous suspensions of Co–Al LDH with varying concentrations of CIP were prepared and examined following the same procedure, as CIP exhibited the highest quenching efficiency for Co–Al LDH. Fluorescence emission quenching (Q) was calculated according to eqn (1), and the fluorescence quenching mechanism was studied employing the Stern–Volmer (S–V) approach as shown in eqn (2).

$$Q\ (\%) = \{(I_0 - I)/I_0\} \times 100 \tag{1}$$

$$I_0/I = 1 + K_{SV}\ [\mathrm{M}] \tag{2}$$

The quenching constant (K_{SV}) depends on the molar concentration ([M]), with I_0 and I representing fluorescence intensities before and after sample addition, respectively.[70–72]

3.2. Photocatalytic ciprofloxacin degradation

Ciprofloxacin (CIP) served as the model pollutant to evaluate the photocatalytic degradation performance of the synthesised materials. For typical experiments, 0.04 g of LN2 : 1 photocatalyst was suspended in 20 mL of aqueous CIP solution with 20 ppm as the initial concentration. The solution underwent magnetic stirring in the dark for 30 minutes prior to solar exposure to establish adsorption–desorption equilibrium. Degradation tests proceeded under ambient sunlight on the rooftop facility of our institute in Bhubaneswar, Odisha, India, in June, with recorded solar irradiance averaging ~856 W m^{-2}. Reactions lasted 90 minutes, with 3 mL samples collected at every 30-minute interval, centrifuged to remove catalyst particles, and analysed for residual CIP (ppm) *via* a UV-1900i spectrophotometer. Degradation efficiency (η) was determined from the formula involving the initial (C_i) and final (C_f) concentrations. All tests involved triplicate runs, reporting averaged results. Reusability tests on LN2 : 1 followed successive cycles under the same protocol and the post-reaction recovery by centrifugation, sequential rinsing with deionised water and ethanol to eliminate surface residues, drying and reapplication.

3.3. Photocatalytic Cresol Red degradation

Cresol Red (CR) served as the model pollutant to evaluate the photocatalytic degradation performance of the synthesised materials. For typical experiments, 0.04 g of LN2 : 1 photocatalyst was suspended in 20 mL of aqueous CR solution with 20 ppm as the initial concentration. The solution underwent magnetic stirring in the dark for 30 minutes prior to solar exposure to establish adsorption–desorption equilibrium. Degradation tests proceeded under ambient sunlight on the rooftop facility of our institute in Bhubaneswar, Odisha, India, in June, with recorded solar irradiance averaging ~856 W m^{-2}. Reactions lasted 90 minutes, with 3 mL samples collected at every 30-minute interval, centrifuged to remove catalyst particles, and analysed for residual CR (ppm) *via* a UV-1900i spectrophotometer. Degradation efficiency (η) was determined from the formula involving the initial (C_i) and final (C_f) concentrations. All tests involved triplicate runs, reporting averaged results. Reusability tests on LN2 : 1 followed successive cycles under the same protocol and the post-reaction recovery by centrifugation, sequential rinsing with deionised water and ethanol to eliminate surface residues, drying and reapplication.

3.4. Photocatalytic hydrogen peroxide production

For photocatalytic H_2O_2 generation, 0.02 g of photocatalyst was suspended in 50 mL of 10% aqueous isopropanol solution, followed by 10-minute sonication for homogeneous dispersion. Reactions occurred in a specialised double-jacketed reactor with water circulation, using a 300 W xenon lamp (λ > 420 nm cutoff) for visible light illumination and constant O_2 bubbling to support 2-electron reduction. Over 90 minutes, 3 mL samples were taken every 30 minutes, centrifuged to isolate the catalyst, then treated with 1 mL each of 0.4 M KI and 0.1 M KHP. After ~20 minutes of incubation to form the yellow I_3^- complex (intensity reflecting H_2O_2 levels), solutions were diluted and absorbance was measured at 350 nm on a UV-1900i spectrophotometer.

4. Electrochemical measurements

For electrode preparation, 5 mg of the catalyst powder was dispersed in 100 mL of methanol, followed by the addition of 5 mL of Aquivion solution as a binding agent. The resulting suspension was ultrasonicated for 10 minutes to achieve a uniform and well-dispersed slurry. The catalyst ink was then drop-cast onto a 1 × 1 cm fluorine-doped tin oxide (FTO) glass substrate and allowed to dry overnight at 60 °C. The obtained uniform catalyst-coated FTO film was employed as the working electrode in subsequent electrochemical analyses. Electrochemical measurements were carried out in a conventional three-electrode configuration, consisting of the prepared FTO film as the working electrode, a platinum wire as the counter electrode, and a saturated calomel electrode as the reference. The electrolyte solution comprised 0.2 M Na_2SO_4, which was purged with nitrogen gas before measurement to eliminate dissolved oxygen. Electrochemical impedance spectroscopy (EIS) and Mott–Schottky (M–S) analyses were performed at an applied potential of 0.2 V using an AC amplitude of 2 mV.

5. Results and discussion

5.1. Material characterisation

X-ray diffraction (XRD) measurements using Cu Kα radiation (λ = 1.5406 Å) on a Panalytical X'Pert Pro diffractometer (5°–80° 2θ range) determined the crystalline phases of all photocatalysts. Fourier-transform infrared (FTIR) spectroscopy on a PerkinElmer Spectrum identified functional groups through

Open Access Article. Published on 08 April 2026. Downloaded on 4/8/2026 8:29:56 PM.
This article is licensed under a Creative Commons Attribution-NonCommercial 3.0 Unported Licence.

molecular vibrations in KBr pellets scanned from 600 to 4000 cm^{-1}. Surface morphology was examined using a Zeiss Gemini SEM450 Field Emission Microscope (FE-SEM) and a JEOL JEM2100 PLUS Transmission Electron Microscope (TEM). Optical properties were assessed with LAMBDA 750 UV-Vis-NIR diffuse reflectance spectroscopy (UV-DRS) over 200–800 nm. Room temperature photoluminescence (PL) spectra were recorded on an EDINBURGH FLS 1000 fluorescence spectrophotometer. Electrochemical measurements utilised Ivium workstations.

5.2. Crystallography study

Using powder XRD, the phase purity, crystal structure and composition of the as-prepared catalysts were investigated. As shown in Fig. 1a, g-C_3N_5 exhibits two distinct peaks. The first peak, which is less intense at 13.1° with the crystal plane (100), is attributed to the hybridisation of sp^2 aromatic substances within the layer with triazole structure, while the second peak, which is more intense at 27.6° with the crystal plane (002), is associated with the in-plane structural packing of the triazine group.[73,74] The XRD pattern of the pristine Co–Al LDH exhibited characteristic diffraction peaks at $2\theta = 20°$, 37.6°, and 39.8°, which correspond to (003), (006), and (009) crystal planes, respectively.[65] These reflections are indicative of the typical layered structure of hydrotalcite-like LDH materials with well-ordered brucite-like layers and interlayer anions.[75] Also, two distinct peaks were observed at 2θ = 11.2° and 21.3°, corresponding to the (003) and (006) planes of the LDH phase, for the LN composites, respectively.[51,76] The intensity variations among the composites reflect the compositional differences. Specifically, LN1 : 1 and LN2 : 1 showed more intense LDH peaks due to the higher loading of Co–Al LDH while keeping g-C_3N_5 constant. In contrast, LN1 : 2, with a higher proportion of g-C_3N_5, exhibited a more intense peak at 27.6°, confirming the dominant presence of g-C_3N_5 in that composite. Notably, the peak at 11.2° was significantly more intense than that at 21.3°, suggesting that the layered structure of LDH was preserved in the composites and that the (003) basal plane remained dominant. This trend supports the successful formation of heterostructures and the tunability of their composition, which is crucial for optimising photocatalytic performance.

FTIR spectra were recorded to explore the characteristic features of Co–Al LDH, g-C_3N_5, and LN composites. All samples exhibited a broad absorption band centred around ~3446.7 cm^{-1}, which corresponds to the OH stretching vibrations of hydroxyl groups and adsorbed/interlayer water molecules, a characteristic feature of LDHs.[77] In the LN composites, several additional peaks appeared in the range of 787–1690 cm^{-1}, which are assigned to the stretching vibrations of CN heterocycles and conjugated structures in the g-C_3N_5 framework.[78,79] These peaks confirm the successful incorporation of g-C_3N_5 into the LDH matrix and the presence of its typical triazine-based structure. Notably, a strong and sharp peak at ~1376.8 cm^{-1} was observed in all LN composites, which is attributed to the bending vibrations of intercalated nitrate (NO_3^-) ions present between the LDH layers.[80] The persistence of this band indicates that the layered structure of LDH remains intact upon hybridisation with g-C_3N_5.

5.3. Raman spectroscopy

Complementing the FTIR study, the structural, vibrational and polymorphous characteristics of the nanocomposites were investigated by Raman spectroscopy. While crystalline specimens show sharp Raman peaks, polycrystalline or amorphous

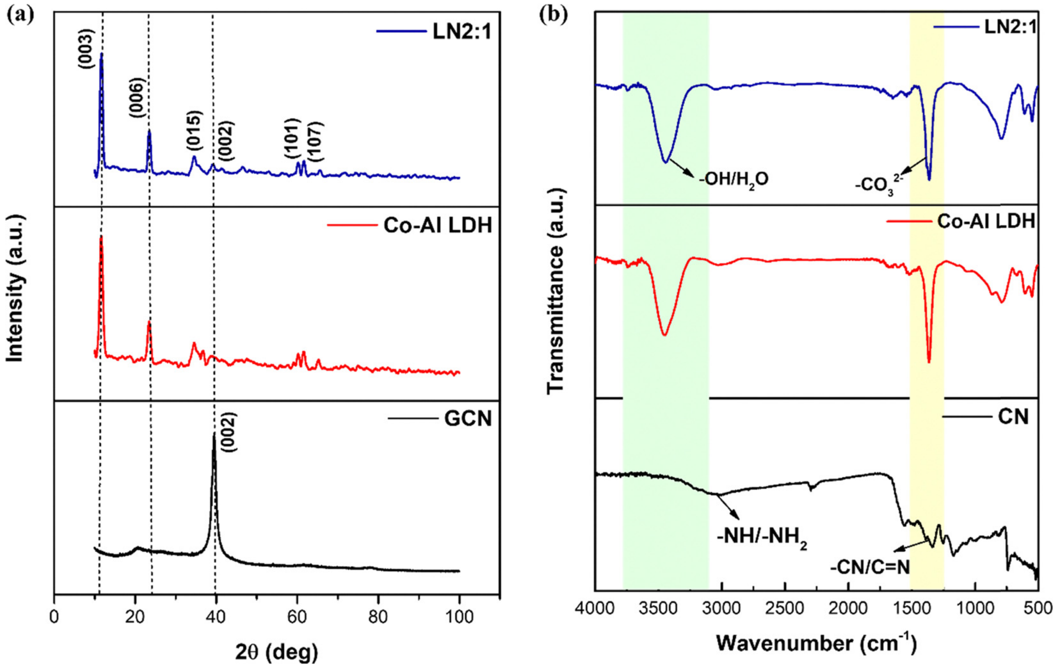

Fig. 1 (a) XRD of Co–Al LDH, g-C_3N_5 and LN2 : 1 and (b) FTIR study of Co–Al LDH, g-C_3N_5 and LN2 : 1.

Open Access Article. Published on 08 April 2026. Downloaded on 4/8/2026 8:29:56 PM. This article is licensed under a Creative Commons Attribution-NonCommercial 3.0 Unported Licence.

materials show wide Raman peaks. Because of the confinement effect of nanocrystalline materials, Raman peaks expand and shift downward. Furthermore, the Raman spectra are noticeably affected by tensile and compressive stresses, which cause a shift towards either shorter wavelengths (blue shift) or longer wavelengths (red shift). Fig. 2a exhibits characteristic vibrational modes confirming the successful formation of the Co–Al LDH structure and the presence of metal–oxygen and hydroxyl coordination environments. The deconvoluted peaks observed at 574.1 cm^{-1} and 628 cm^{-1} correspond to the M–O (Co–O and Al–O) lattice vibrations within the brucite-like layers, indicating strong metal–oxygen bonding and structural integrity of the Co–Al LDH framework.[81,82] The most intense and sharp peak at 718 cm^{-1} is attributed to the symmetric stretching vibrations of Co–O–Al linkages, which further confirms the formation of a well-ordered layered double hydroxide structure through octahedral coordination of metal cations with hydroxyl groups.[82] The peak at 266.1 cm^{-1} in Fig. 2b is attributed to lattice vibrational modes associated with metal–oxygen interactions in the LDH layer, while the prominent bands at 487.3 cm^{-1} and 621.86 cm^{-1} correspond to Co–O and Al–OH bending vibrations, confirming the structural integrity of the brucite-like layers.[83] The peak at 692.1 cm^{-1} indicates M–O–M (metal–oxygen–metal) stretching vibrations, which further validate the layered double hydroxide framework.[84] The broad and intense band at 1333.56 cm^{-1} is assigned to the characteristic stretching vibrations of C–N and heptazine units in g-C_3N_5, signifying the presence of a polymeric carbon nitride structure.[78] The deconvoluted peaks demonstrate good fitting accuracy, indicating well-defined vibration modes and strong interfacial interaction between LDH layers and g-C_3N_5.[85] The sharp peak at 690 cm^{-1},[86] as shown in Fig. 2c, corresponds to the Co–O stretching or lattice deformation mode of Co–Al LDH, suggesting a highly ordered crystalline structure and strong vibrational activity in this region. The peaks at 488 cm^{-1} and 625 cm^{-1} are often assigned to Co–O–Al bending or stretching of LDH into the local bonding environment and phase composition of the LN2 : 1 composite.[87,88] Fig. 2d shows that the intense band centred at 1392 and 1433 cm^{-1} dominates the spectrum of the LN1 : 2 composite, reflecting the C–C sp^3 hybridised D-band region and C=N or C–N heterocycles, which confirms the presence of conjugated heptazine/triazine rings.[89] The peaks at lower shifts (1056–1319 cm^{-1})[90] and higher shifts (1528, 1578 cm^{-1})[91] suggest the presence of multiple phases, functional groups, or defect sites, highlighting the complex nature of LN1 : 2.

5.4. Morphological studies

The microstructural characteristics and surface architecture of Co–Al LDH, g-C_3N_5, and the LN2 : 1 composite were elucidated

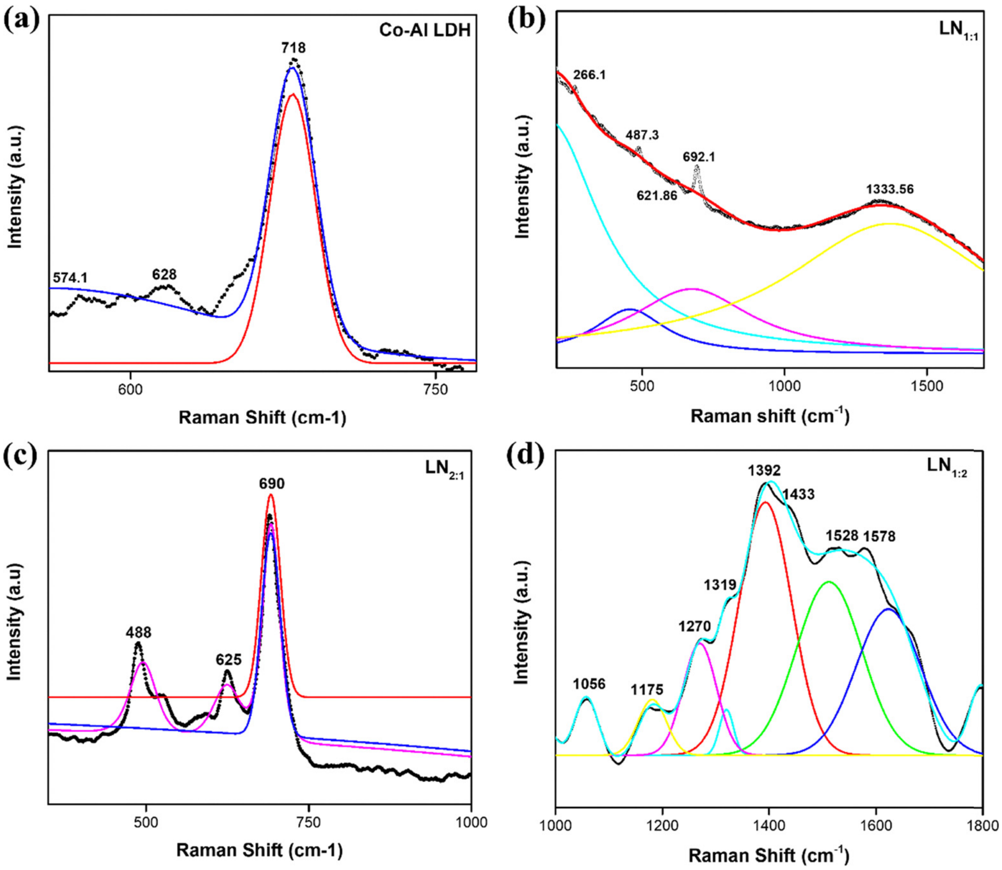

Fig. 2 Raman spectroscopy of Co–Al LDH and LN nanocomposites.

Open Access Article. Published on 08 April 2026. Downloaded on 4/8/2026 8:29:56 PM.
This article is licensed under a Creative Commons Attribution-NonCommercial 3.0 Unported Licence.

utilising a combination of FE-SEM, TEM, HR-TEM, and EDAX techniques. FE-SEM images of Co–Al LDH (Fig. 3a) revealed that Co–Al LDH is composed of uniformly dispersed nano-platelets, highlighting its intrinsic layered configuration.[92] Conversely, high-magnification observations of pristine g-C_3N_5 (Fig. 3c) uncovered a classic nanosheet morphology, marked by a smooth surface and partially frayed edges.[93] This distinct structure is attributed to the thermal condensation polymerisation conducted at elevated temperatures, followed by ultrasonic exfoliation, which imparts both flexibility and high aspect ratio to the nanosheets.[79] The LN2 : 1 composite, examined *via* both FE-SEM and HR-TEM (Fig. 3b and d), exhibited an interplanar sheet-like morphology, signifying the integration of g-C_3N_5 with Co–Al LDH. HR-TEM analysis (Fig. 3e) disclosed well-defined lattice fringes corresponding to each component, indicating the coexistence of multiple crystalline phases in the heterogeneous nanocomposite.[94] The SAED pattern (Fig. 3f) and EDAX analysis shown in Fig. 3g further validated the presence of specific diffraction planes, confirming structural intergrowth and phase purity and homogeneous distribution of the elements present in the LN2 : 1 nanocomposite.[95]

5.5. X-ray chemical state and surface composition analysis

The X-ray photoelectron spectroscopy (XPS) analysis was carried out to investigate the elemental composition and surface chemical states of the synthesised Co–Al LDH/g-C_3N_5 nanocomposite, as shown in Fig. 4a. The survey spectrum confirms the presence of Co, Al, N, O, and C elements, verifying the successful integration of Co–Al LDH with g-C_3N_5 and the absence of any impurity peaks. The high-resolution Co 2p spectrum (Fig. 4b) exhibits two main peaks at around 780 eV (Co $2p_{3/2}$) and 795 eV (Co $2p_{1/2}$) along with satellite features, indicating the coexistence of Co^{2+} and Co^{3+} species, which supports mixed-valence states in the LDH layers.[96] The O 1s spectrum can be deconvoluted into peaks centred near 530 eV, corresponding to metal–oxygen bonds (M–O), and around 531–532 eV, assigned to hydroxyl groups (M–OH) and adsorbed water on the surface (Fig. 4f).[97] The N 1s spectrum in Fig. 4e shows peaks near 398.5–400 eV attributed to C=N–C and C–N–C linkages originating from the g-C_3N_5 framework, confirming its presence in the composite.[98] The C 1s spectrum in Fig. 4d reveals components at 284.6 eV (C–C/C=C), 286.2 eV (C–N/C–O), and 288.3 eV (N–C=N), representing graphitic and heteroatom-bonded carbon environments.[99] The Al 2p signal observed near 74.12 eV and 74.8 eV, as shown in Fig. 4c, corresponds to Al^{3+} species in the LDH lattice.[100] Overall, the XPS results validate the successful formation of the Co–Al LDH/g-C_3N_5 heterostructure with mixed oxidation states of cobalt, hydroxyl-rich LDH surfaces, and strong interfacial coupling between the LDH and g-C_3N_5 components, which are beneficial for enhanced charge separation and catalytic activity.

5.6. Optical studies

To explore the optical properties, the UV-DRS spectra of g-C_3N_5, Co–Al LDH and the LN composites were studied (Fig. 5a). When the heterostructure with Co–Al LDH forms, there is no

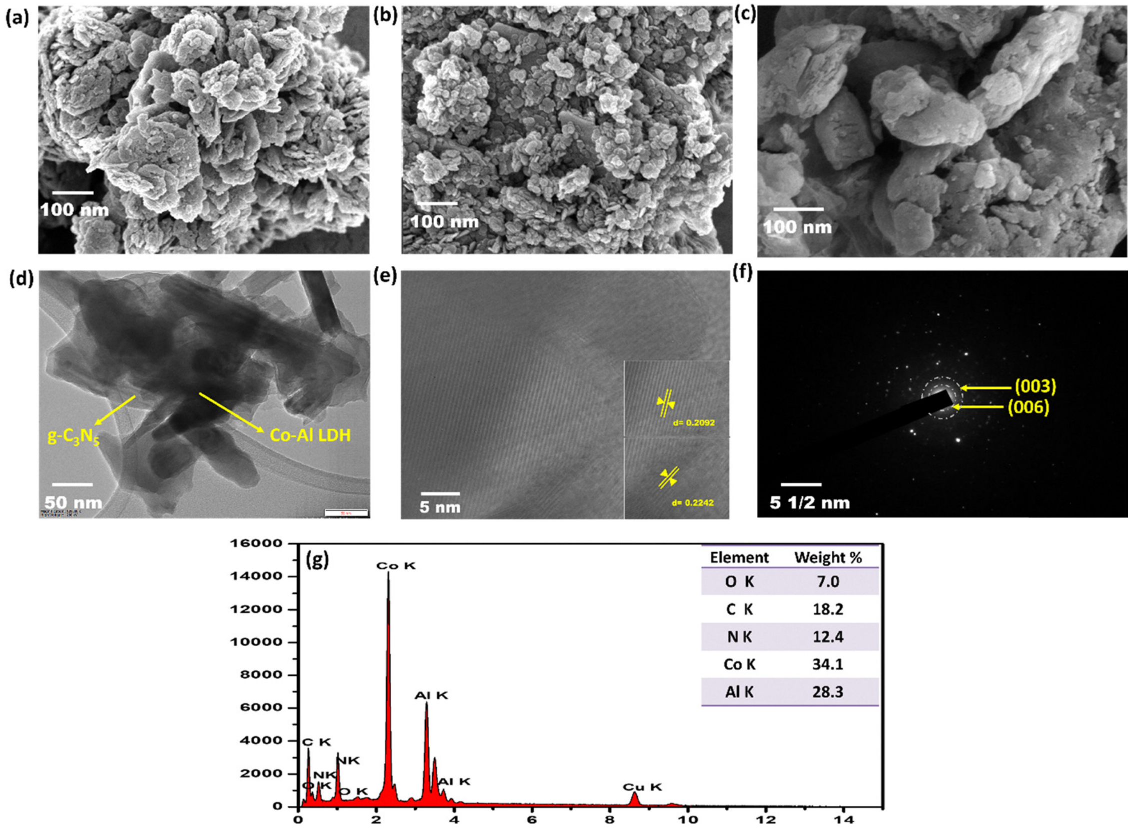

Element	Weight %
O K	7.0
C K	18.2
N K	12.4
Co K	34.1
Al K	28.3

Fig. 3 (a) FE-SEM of Co–Al LDH, (b) FE-SEM of LN2 : 1, (c) FE-SEM of g-C_3N_5, (d)–(f) HR-TEM of LN2 : 1 and (h) EDAX analysis of LN2 : 1.

Open Access Article. Published on 08 April 2026. Downloaded on 4/8/2026 8:29:56 PM.
This article is licensed under a Creative Commons Attribution-NonCommercial 3.0 Unported Licence.

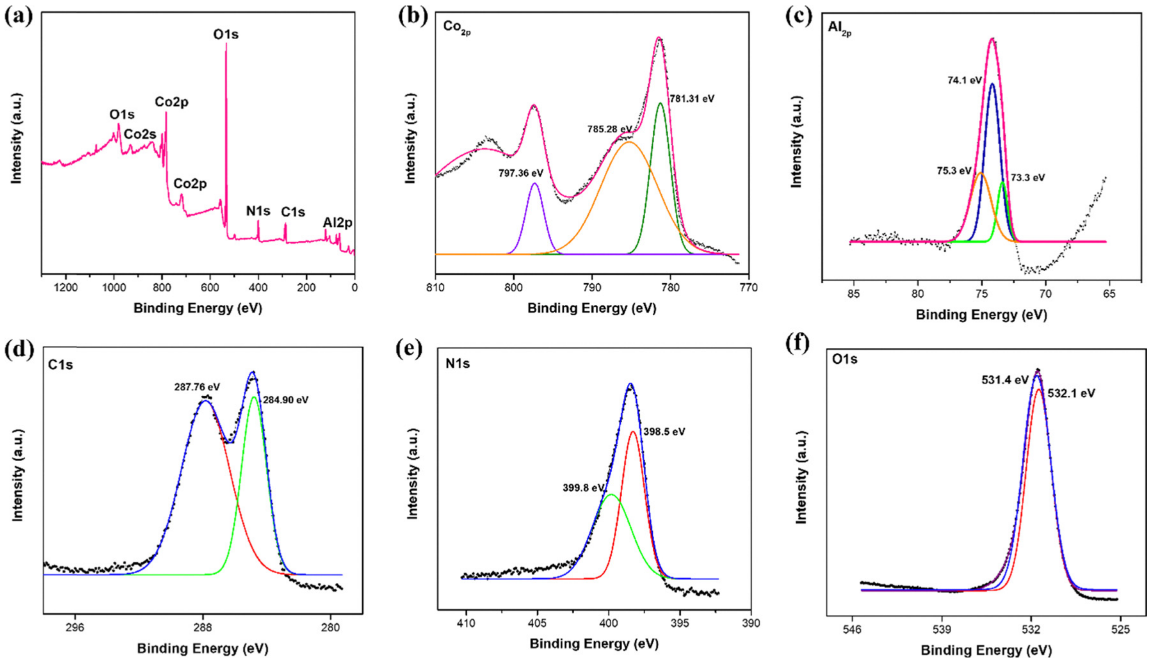

Fig. 4 (a) XPS survey of LN2 : 1, (b) Co 2p, (c) Al 2p, (d) C 1s, (e) N 1s, and (f) O 1s XPS spectra.

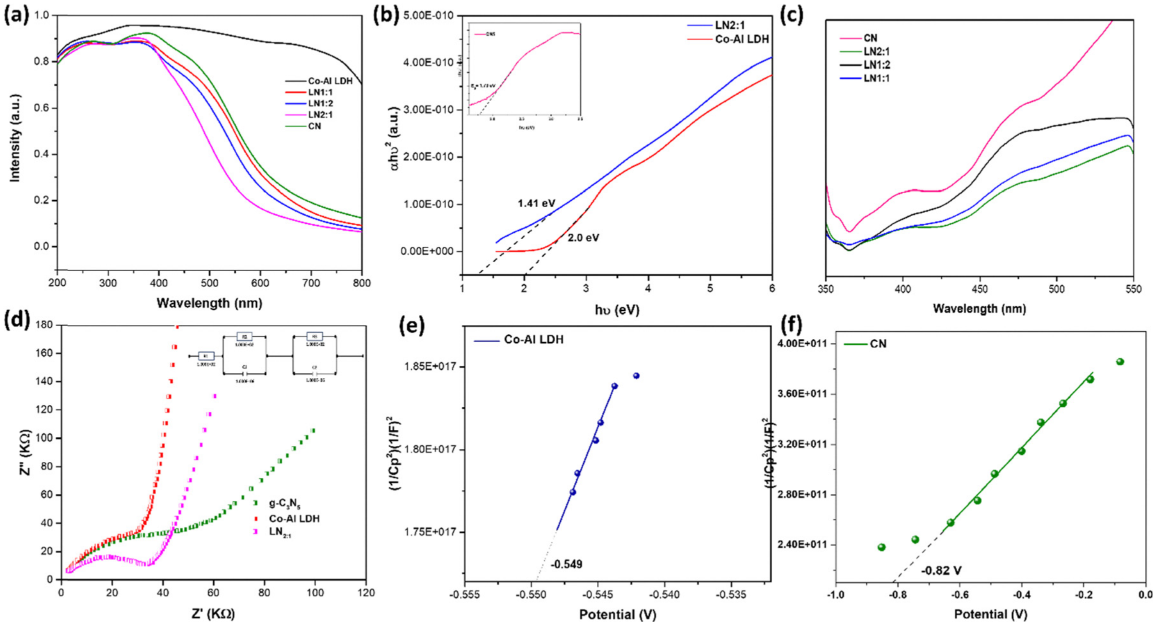

Fig. 5 (a) UV-DRS spectra, (b) Tauc plots for bandgaps of g-C_3N_5, LN2 : 1 and Co–Al LDH, (c) PL spectra of g-C_3N_5, LN2 : 1, LN1 : 2 and LN1 : 1, (d) EIS Nyquist plots, and (e and f) Mott–Schottky plots of as-prepared catalysts.

significant change in the absorption edge, and a sharp adsorption edge of about 560 nm is observed in the case of g-C_3N_5.[101] According to the Tauc plots (Kubelka–Munk) shown in Fig. 5b, the calculated optical bandgaps of g-C_3N_5, Co–Al LDH and the LN2 : 1 composite are 1.79,[64] 2.0[65] and 1.41 eV, respectively, based on eqn (3). Fig. S5 shows the bandgaps of the other LN composites.

$$(\alpha h\nu^{\gamma}) = \beta(h\nu - E_g) \qquad (3)$$

The bandgap energy (E_g) of a material can be estimated using the Tauc plot by analysing the relationship between (h) and photon energy. In this context, α represents the absorption coefficient, h is Planck's constant, ν denotes the frequency of the incident light, β is a proportionality constant, E_g is the bandgap energy in electron volts (eV), and γ indicates the type of electronic transition (γ = 2 corresponds to an allowed indirect transition and $\gamma = \frac{1}{2}$ corresponds to an allowed direct transition).[102]

Open Access Article. Published on 08 April 2026. Downloaded on 4/8/2026 8:29:56 PM.
This article is licensed under a Creative Commons Attribution-NonCommercial 3.0 Unported Licence.

The interfacial charge transfer characteristics of Co–Al LDH, g-C_3N_5 and LN2 : 1 were investigated using electrochemical impedance spectroscopy (EIS). Fig. 5d illustrates the Nyquist plots, which show the imaginary component of impedance (Z'') in relation to the real component (Z'). At the electrode–electrolyte interface, a smaller arc radius in the Nyquist plot usually indicates a lower charge transfer resistance, indicating more effective separation and migration of photogenerated charge carriers.[103] The g-C_3N_5 catalyst has the largest semicircular arc among the samples, which means it has the most barrier to charge transfer and, as a result, the least effective interfacial charge transfer.[104] An intermediate charge transfer resistance is reflected in the LDH sample's moderate arc radius.[105] Among the three, the LN2 : 1 composite has the shortest arc, which is indicative of the lowest charge transfer resistance.[106] This small but noticeable decline in the charge transfer resistance of LN2 : 1 demonstrates the synergistic effect of the heterostructure formation, which is attributed to the interaction of Co–Al LDH and g-C_3N_5, facilitating quick charge separation and transfer.[66] The direct Z-scheme charge transfer channel, which efficiently suppresses the charge carrier recombination and maintains their high redox potentials, is responsible for the improved interfacial charge dynamics.[107] As shown in the inset of Fig. 5d, an equivalent circuit model was used to quantitatively assess the impedance data. A capacitance (C), a constant phase element (CPE), a series resistance (R_1), and a parallel resistance (R_2) constitute the circuit. The solution resistance is represented by the R_1 value (1.000×10^2 Ohm), while the polarisation resistance related to charge transfer at the interface is represented by the R_2 value (1.000×10^{-6} Ohm); C_1 and C_2 values were found to be 1.000×10^{-2} Ohm (as shown in the circuit inside in Fig. 5d). The interaction of LDH with CN is probably the cause of this decline in charge transfer resistance for LN2 : 1, which suggests improved electrical communication between the semiconductor surfaces.[108] Faster migration and separation of photogenerated charge carriers may be supported by such an interface.

These preliminary EIS results suggest that the LN2 : 1 structure may promote improved photocatalytic performance; the exact charge transfer mechanism is discussed in a subsequent section.[66] PL spectra provide additional evidence for effective charge separation by displaying a decreased emission intensity of LN2 : 1, indicating a lower rate of charge carrier recombination.[109] The combined results of EIS and PL clearly suggest that the nanocomposite arrangement improves interfacial charge dynamics, setting the stage for better performance in ensuing photocatalytic applications.[101]

Mott–Schottky (MS) analysis was carried out on pure Co–Al LDH and g-C_3N_5 to determine their semiconductor type and estimate their conduction band (CB) edge potentials to supplement the optical absorption and bandgap data acquired from UV-Vis diffuse reflectance spectroscopy (UV-DRS).[109] Both Co–Al LDH and g-C_3N_5 absorb well in the visible spectrum, according to the UV-DRS data, which is beneficial for photocatalytic applications in their composite system. The Mott–Schottky plots for both Co–Al LDH and g-C_3N_5 display positive slopes, indicative of n-type semiconductors. This n-type behaviour, which is characteristic of metal hydroxides like Co–Al LDH and polymeric carbon nitrides like g-C_3N_5, shows that electrons compose the bulk of the charge carriers in these semiconductors. Flat-band potentials, which for n-type semiconductors nearly resemble the conduction band minimum, were found from the intercepts of the Mott–Schottky plots. Fig. 5e and f show that the CB edge for g-C_3N_5 was around −0.83 V *vs.* NHE, whereas the CB edge for Co–Al LDH was calculated to be −0.549 V *vs.* NHE.

To predict the kinetics of charge transfer in their composite photocatalyst system, these CB positions are crucial. While Co–Al LDH's more positive CB makes it appropriate for receiving electrons or aiding in charge separation, g-C_3N_5's greater negative CB indicates that it has superior thermodynamics for reduction processes. Eqn (4) was used to determine the valence band (VB) edge potentials to finish the electronic band structure analysis:

$$\mathrm{VB} = E_\mathrm{g} - \mathrm{CB} \tag{4}$$

where E_g is the optical bandgap energy, E_VB is the valence bandgap edge potential (V *vs.* NHE), and E_CB is the conduction band edge potential (V *vs.* NHE). The calculated bandgap energies of g-C_3N_5 and Co–Al LDH were 1.79 eV and 2.0 eV, respectively, based on the Tauc plots. The corresponding E_VB were found to be 1.46 V and 0.96 V for Co–Al LDH and g-C_3N_5, using the previously found E_CB values. This band alignment indicates that the photogenerated electrons may lose redox potential when incorporated into a heterojunction if direct electron transfer takes place from g-C_3N_5 to Co–Al LDH. The two semiconductors most likely function *via* a Type-II mechanism, where the VB holes of g-C_3N_5 and the CB electrons of Co–Al LDH recombine internally, maintaining the strong redox ability of the electrons in g-C_3N_5 and the holes in Co–Al LDH, according to the analysis in later sections of reactive species and photocatalytic performance. This band alignment provides a foundation for the improved photocatalytic performance seen in later analysis, with supportive, effective charge separation and redox activity in the composite system.

5.7. N_2 sorption analysis

Brunauer–Emmett–Teller (BET) analysis reveals the specific surface area, pore volume, and adsorption behaviour of g-C_3N_5, Co–Al LDH and LN composites. The N_2 adsorption–desorption isotherm (Fig. 6a) displays a typical Type-IV profile with H3 hysteresis loops, confirming the mesoporous nature of the materials.[110] The pristine g-C_3N_5 shows the lowest adsorption volume, indicating a smaller surface area and limited porosity.[111] In contrast, Co–Al LDH demonstrates the highest uptake, particularly in the high relative pressure region ($P/P_0 >$ 0.8), signifying a larger surface area and significant pore volume, with contributions from mesopores.[112] The LN2 : 1 composite exhibits intermediate adsorption behaviour, with higher uptake than pure g-C_3N_5, suggesting that coupling g-C_3N_5 with Co–Al LDH enhances porosity and surface area while maintaining structural stability.[113] The sharp increase at

Open Access Article. Published on 08 April 2026. Downloaded on 4/8/2026 8:29:56 PM.
This article is licensed under a Creative Commons Attribution-NonCommercial 3.0 Unported Licence.

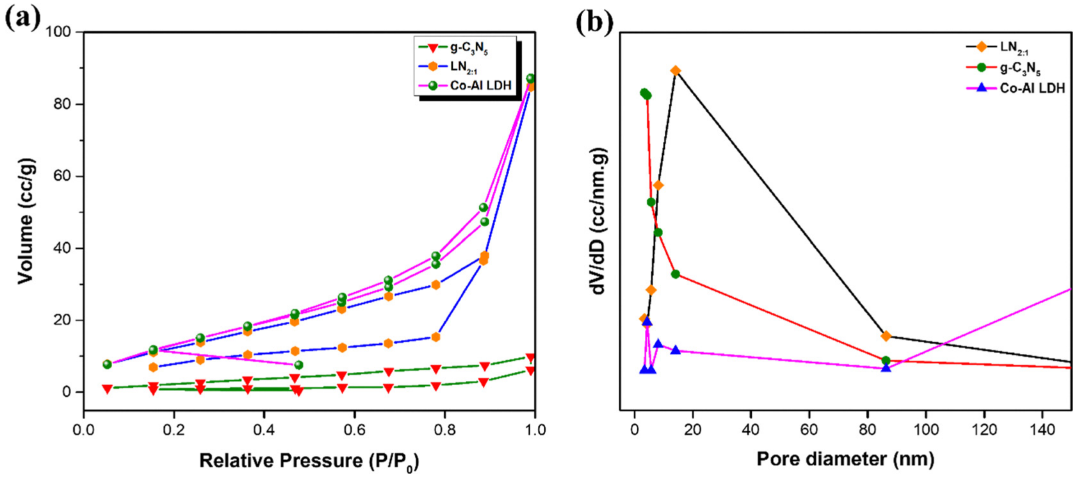

Fig. 6 (a) N_2 adsorption–desorption isotherm and (b) BJH-pore size distribution curve of Co–Al LDH, g-C_3N_5 and LN2 : 1.

high P/P_0 for LN2 : 1 confirms the presence of larger pores or interparticle voids, whereas the gradual slope of g-C_3N_5 indicates its relatively compact structure.[114] These differences directly reflect the textural modifications induced by composite formation, which increase accessible active sites and improve molecular diffusion pathways, essential for efficient photocatalytic performance.[115] The BJH-PSD graph (as shown in Fig. 6b), reveals the pore size range and dominant pore structure of a material, which provide insight into its pore structure.[116,117] All three materials exhibit pore size predominantly within the mesoporous range (2–50 nm), consistent with the adsorption–desorption isotherm.[117] Pure g-C_3N_5 shows only weak and narrow contributions in the low pore diameter region, indicating a low pore volume and relatively compact structure with limited mesoporosity.[111,118] In contrast, Co–Al LDH displays a broader pore distribution with significant pores below 10 nm and a gradual tail extending towards larger diameters (>80 nm), suggesting the coexistence of mesopores with interparticle macropores.[119] The LN2 : 1 composite exhibits a distinct and intense peak centred in the mesoporous region (∼10–20 nm), accompanied by additional contributions across a wider diameter range, reflecting the formation of a hierarchical pore network.[120] The enhanced pore volume and well-developed mesoporosity in LN2 : 1 compared to pristine g-C_3N_5 indicate that the introduction of Co–Al LDH not only increases surface accessibility but also prevents the stacking of g-C_3N_5 layers, thereby generating more open textural frameworks.[121] The hierarchical distribution is advantageous, as mesopores facilitate efficient reactant diffusion, while larger pores act as reservoirs, ensuring enhanced accessibility of active sites and improved photocatalytic efficiency.[122] Table 1 shows the surface area, pore diameter and pore volume of Co–Al LDH, g-C_3N_5 and LN2 : 1, and Table 2 provides a list of catalysts used in pollutant degradation.

Table 1 The surface characteristics of the as-synthesised materials

Sl. No.	Catalyst	Surface area (m^2 g^{-1})	Pore volume (cc g^{-1})	Pore diameter (nm)
1	Co–Al LDH	16.109	0.048	3.36
2	g-C_3N_5	2.066	0.015	3.36
3	LN2 : 1	19.463	0.124	3.35

6. Photocatalytic assessment of the LN composite

6.1. Photocatalytic degradation of CIP

As shown in Fig. 7a, the photocatalytic activity of the synthesised catalysts Co–Al LDH, g-C_3N_5, LN1 : 1, LN2 : 1, and LN1 : 2 in breaking down CIP under solar light was assessed. To achieve adsorption–desorption equilibrium with the catalysts, CIP underwent a 30-minute dark reaction before being exposed to light for 120 minutes. The trend was followed by the photocatalytic degradation efficiency: LN2 : 1 > LN1 : 1 > LN1 : 2 > Co–Al LDH > g-C_3N_5. Its subsequent degradation was made easier by the enhanced interaction and adsorption of CIP on Co–Al LDH which was supported by g-C_3N_5.

Since the pH of the solution affects several variables that affect the photodegradation efficiency of CIP, it is essential to optimise the effects of photocatalysis. As shown in Fig. 7b, a pH range of 3 to 9 was investigated to analyse the effects of the initial values on the degradation process. The findings demonstrated that photodegradation efficiency increased with solution pH up to 5, at which point it started to decrease. The electrostatic interactions between the catalyst surface, CIP, substrates, and the charged radicals produced during the reaction are among the many elements that go into understanding how pH affects photocatalysis. Depending on the pH environment, these interactions can either enhance or hinder the photocatalytic process. Because surface hydroxyl groups dissociate and contribute to negative charges through deprotonation, LDH normally has a positive surface charge at neutral pH. The PZC of the LN2 : 1 composite was determined to be 5.5, indicating that the surface charge stays negative at this pH. CIP is a zwitterion at neutral pH. At pH 7, the nitrogen in the piperazine ring (pK_a ∼ 8.7) remains protonated, carrying a positive charge, but the carboxyl group of

Open Access Article. Published on 08 April 2026. Downloaded on 4/8/2026 8:29:56 PM.
This article is licensed under a Creative Commons Attribution-NonCommercial 3.0 Unported Licence.

Table 2 List of catalysts

Catalyst	Bandgap (eV)	Pollutant	Mechanism	Degradation efficiency	Ref.
ZnAl LDH/g-C_3N_4	~2.5	Ciprofloxacin	Z-Scheme	>90%	123
g-C_3N_4/ZnFe LDH + Oxone	~2.7	Tetracycline	Heterojunction	~95%	124
Ni–Fe LDH (photo-Fenton)	2.0–3.4	Tetracycline	Photo-Fenton	99.11%	125
g-C_3N_4/NiFe LDH	~2.7	H_2 evolution, tetracycline	Type-II	—	126
Zn–Fe LDH/rGO/g-C_3N_5	~2.5	Ciprofloxacin	Z-Scheme	95%	127
Mg–Al LDH@g-C_3N_4@Ag_3PO_4	~2.7	Methylene blue	Synergistic	99%	128
Fe_2O_3/g-C_3N_5	<2.7	Tetracycline	Z-Scheme	92.46%	129
Ni–Cr LDH/g-C_3N_5	2.52	Rhodamine B, water splitting	Type-II	—	66
Co–Al LDH/g-C_3N_5	1.41	Ciprofloxacin, Cresol Red dye	Type-II	92.1%	This work

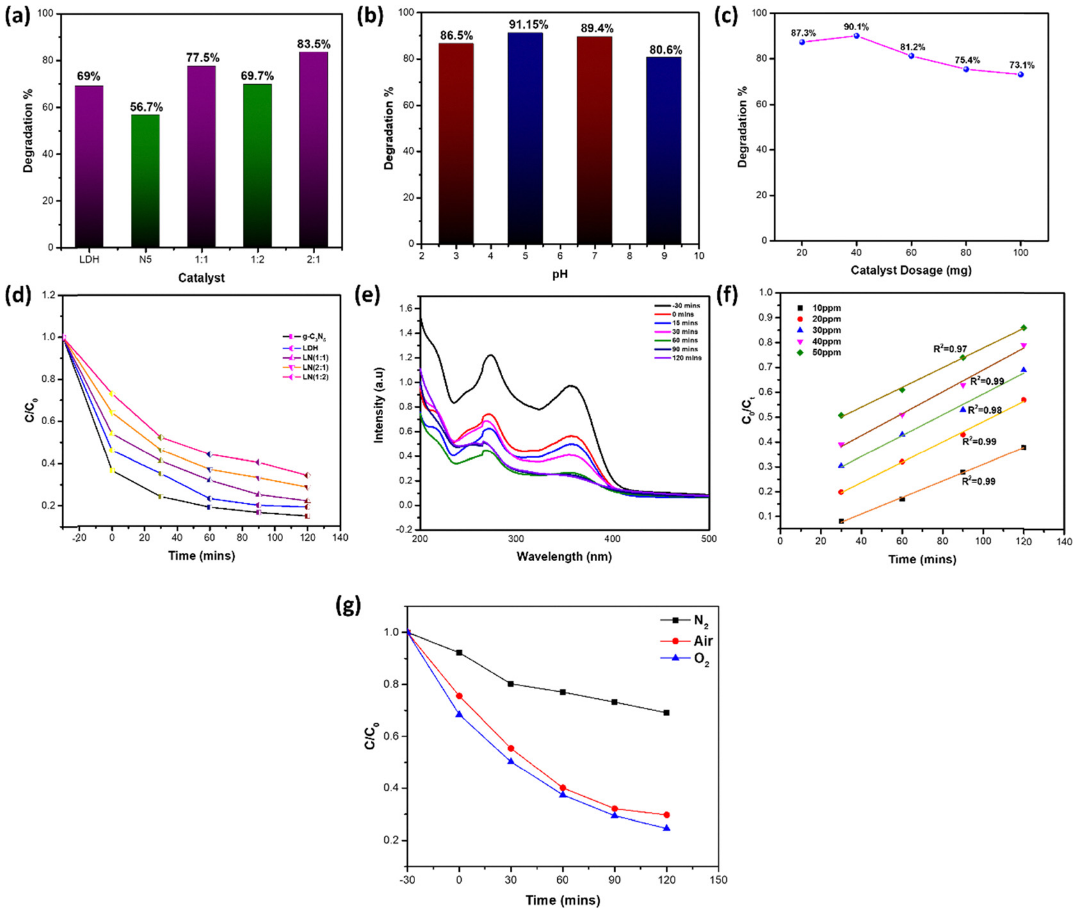

Fig. 7 (a) Effect of various catalysts, (b) effect of solution pH (3, 5, 7, and 9), (c) effect of catalyst dosage (10 mg, 20 mg, 30 mg, 40 mg, and 50 mg), (d) effect of solution concentration (10–50 ppm) with different time intervals (every 30-minute interval), (e) absorbance with time, (f) photocatalytic degradation kinetics of CIP of various concentrations with time by the LN2 : 1 catalyst and (g) effect of the presence of O_2.

CIP (pK_a *vs.* 5.9) deprotonates, carrying a negative charge. In addition to electrostatic forces, the zwitterionic form of CIP enables further advantageous interactions with the catalyst surface through hydrogen bonding, hydrophobic interactions, and possibly π–π stacking interactions between the aromatic rings of CIP and the catalyst surface. The capacity of CIP's functional groups to create hydrogen bonds with the catalyst surface at pH 7 further improves the interaction between CIP and the catalyst. Through interactions with the catalyst's hydroxyl and amine groups, the carboxyl group can function as a hydrogen bond acceptor and the amine group as a donor. Furthermore, CIP is probably most soluble at neutral pH, which enhances its adsorption on the catalyst surface and encourages a more effective photodegradation pathway. On the other hand, CIP solubility may decline at basic or acidic pH values, which might result in less efficient breakdown and less adsorption.[104,130]

Several operational parameters are crucial for adjusting the response rate and enhancing the photocatalytic effectiveness. Various amounts of catalyst (ranging from 0.02 to 0.1 g) were added to the reaction medium. As shown in Fig. 7c, the

Open Access Article. Published on 08 April 2026. Downloaded on 4/8/2026 8:29:56 PM.
This article is licensed under a Creative Commons Attribution-NonCommercial 3.0 Unported Licence.

degradation rate increased dramatically when the catalyst dosage increased from 0.02 to 0.04 g, reaching 90.1% at 120 minutes. However, the pace of disintegration decreases after this, which could be because of a decreased capacity to capture light. Aggregation occurs when catalyst concentration increases, lowering exposure to visible light and, hence, photocatalytic activity.

Additionally, as shown in Fig. 7d, the impact of CIP concentration on the photocatalytic degradation pathway was investigated. After photodegradation, the absorbance for 0.1 to 0.5 g L^{-1} of CIP solution was measured at different time intervals of 0, 30, 60, 90, and 120 minutes using a wavelength range of 200–380 nm. The absorbance peak at 275 nm, which corresponds to CIP, gradually declined over time, as shown in Fig. 7e. The maximum degradation efficiency was achieved at 120 minutes of exposure, which was the same for all investigations. Furthermore, as shown in Fig. 7f, the CIP degradation rate over time followed pseudo-1st order kinetics.

Fig. 7f, where the degradation kinetics are shown as C_0/C_t *vs.* time, shows the interaction between the initial concentration of CIP (C_0) and its concentration at a certain time (C_t). The degradation efficiency was assessed using the pseudo-first-order kinetics-corresponding apparent rate constant (K_{app}). According to the first-order kinetics model, the K_{app} value of LN2 : 1 was 0.0155 min^{-1}, around 1.7 times greater than that of pristine LDH (0.009 min^{-1}) and 1.38 times more than that of pristine g-C_3N_5 (0.0112 min^{-1}). Additionally, when the initial CIP concentration increases, the K_{app} value decreases, suggesting a reduction in the rate of degradation at higher concentrations. Table 3 provides a good summary of these developments. In order to affirm the mechanistic function of molecular oxygen in the photodegradation of CIP, experiments using LN2 : 1 were conducted. As shown in Fig. 7g, the catalyst displayed a progressive decline in the concentration of CIP in ambient air, demonstrating strong activity under typical conditions. The concentration dropped dramatically after the addition of O_2 in the system, after 120 min, highlighting the increased formation of superoxide radicals and the crucial role played by oxygen in the entire process. On the other hand, under N_2-purged conditions, a notable decline in photocatalytic activity was noted, demonstrating the necessity of dissolved oxygen for the enhanced photo-degradation performance.

6.2. Photoluminescence sensing

6.2.1. Solvent selection for Co–Al LDH, LN2 : 1, and g-C_3N_5.

This study investigated the influence of different solvents on the fluorescence properties of Co–Al LDH, LN2 : 1, and g-C_3N_5. To evaluate the effectiveness in detecting various antibiotics, including CAP, NFX, NFT, NPX, CIP OFL, MTZ, RXM, COL, and RBF, 4 mg of Co–Al LDH, LN2 : 1, and g-C_3N_5 powder was dispersed in 5 mL of a range of organic solvents, namely acetone, water (H_2O), dimethylformamide (DMF), diethylformamide (DEF), tetrahydrofuran (THF), chloroform ($CHCl_3$), dichloromethane (DCM), acetonitrile (CH_3CN), isopropanol (IPA), methanol (MeOH), and nitrobenzene (NB). The suspensions were sonicated for 30 minutes to ensure uniform dispersion and maximise solvent interaction, followed by equilibration for 24 hours. Luminescence spectra were recorded at room temperature using an excitation wavelength of 300 nm, with an emission range of 200–600 nm. Co–Al LDH, LN2 : 1, and g-C_3N_5 suspensions exhibited solvent-dependent fluorescence behaviour, with both emission intensity and quenching efficiency varying significantly across solvents. Notably, the highest emission intensity was observed for the aqueous, ethanolic and aqueous suspension of LN2 : 1, Co–Al LDH, and g-C_3N_5, respectively (Fig. 8 and Fig. S1, S2).

6.2.2. Selective detection of antibiotics. The luminescence response of Co–Al LDH, LN2 : 1, and g-C_3N_5 was examined against a series of commonly used antibiotics, including chloramphenicol (CAP), ciprofloxacin (CIP), norfloxacin (NFX), nitrofurantoin (NFT), ofloxacin (OFL), naproxen (NPX), metronidazole (MTZ), colchicine (COL), roxithromycin (RXM), and riboflavin (RBF). Prior to use, Co–Al LDH, LN2 : 1, and

Table 3 Rate constant (in min^{-1}) and regression coefficient (R^2) for various concentrations of CIP obtained from the kinetic study, suggesting pseudo-first-order kinetics

Ciprofloxacin drug concentration (ppm)	Time (min)	K_{app} (min^{-1})	Regression coefficient (R^2)
10	120	0.147	0.99
20	120	0.190	0.99
30	120	0.219	0.98
40	120	0.285	0.99
50	120	0.341	0.97

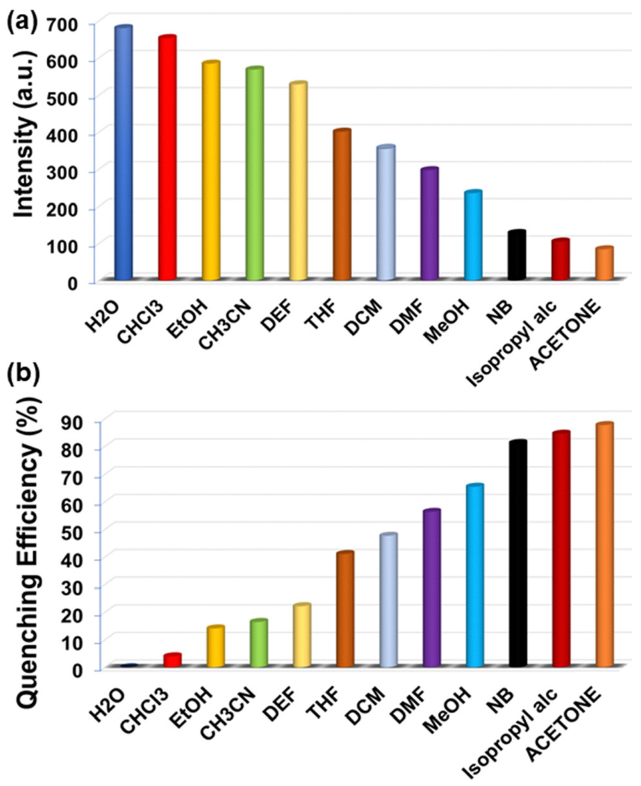

Fig. 8 (a) Fluorescence intensity measurements of LN2 : 1 in different solvent solutions and (b) comparative quenching efficiencies of LN2 : 1 in solvent solution.

Open Access Article. Published on 08 April 2026. Downloaded on 4/8/2026 8:29:56 PM. This article is licensed under a Creative Commons Attribution-NonCommercial 3.0 Unported Licence.

$g\text{-}C_3N_5$ were activated by immersion in methanol for 24 hours, followed by vacuum drying at 30 °C for 24 hours. This pretreatment enhanced surface accessibility and active site exposure, thereby improving fluorescence-based detection.[131–133] The quenching efficiencies of LN2 : 1 toward RXM, NPX, CAP, COL, OFL, NFT, MTC, RBF, NFX and CIP were determined to be 3.82%, 9.41%, 14.11%, 25.14%, 26.76%, 39.26%, 44.70%, 57.51%, 83.97%, and 96.61%, respectively (Fig. 9a and b). The quenching efficiencies of Co–Al LDH towards COL, MTC, NFX, RXM, OFL, CIP, NPX, RBF, CAP and NFT were determined to be 6.80%, 9.17%, 15.03%, 22.78%, 34.65%, 37.02%, 45.41%, 45.88%, 70.72%, and 84.81%, respectively (Fig. S3a and b). For $g\text{-}C_3N_5$, the quenching efficiencies towards antibiotics MTC, OFL, COL, CIP, CAP, NFT, RXM, NFX, RBF, and NPX were 6.48%, 9.10%, 12.34%, 22.06%, 29.62%, 36.88%, 50.30%, 58.64%, 64.35%, and 75.46%, respectively (Fig. S4a and b). Among these, LN2 : 1 demonstrated outstanding sensitivity toward CIP antibiotics, exhibiting the highest quenching efficiency.

For further investigation, an aqueous solution containing 1 mM CIP antibiotic was prepared. A gradual decrease in the fluorescence intensity of LN2 : 1 was observed, suggesting an interaction that suppresses its emission. Fluorescence detection experiments were then performed to evaluate the sensitivity of LN2 : 1 toward CIP antibiotics. As illustrated in Fig. 10, a concentration-dependent quenching effect was evident, with fluorescence intensity progressively decreasing as the concentration of CIP increased. The association amongst the concentrations of CIP antibiotics and the related fluorescence response was examined using the Stern–Volmer (SV) equation ($I_0/I = 1 + K_{SV}$ [M]).[134,135]

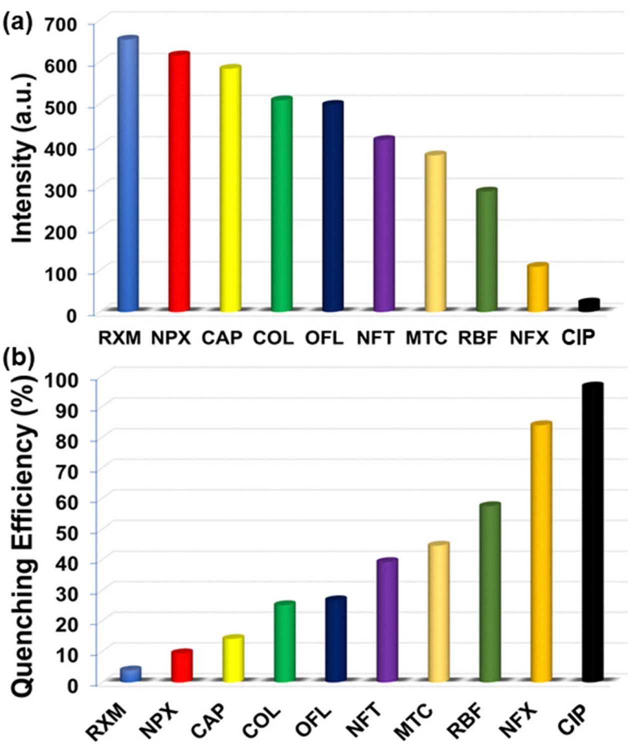

Fig. 9 (a) Fluorescence intensity measurements of LN2 : 1 in different antibiotic solutions and (b) comparative quenching efficiencies of LN2 : 1 in solvent solution with specific antibiotics.

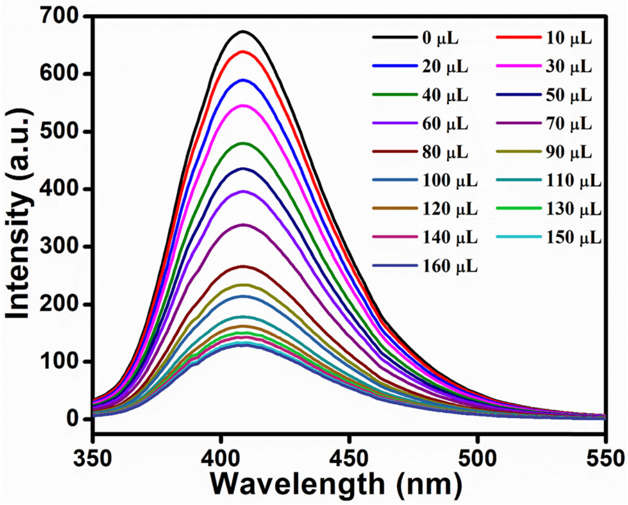

Fig. 10 Variation in the fluorescence intensity of LN2 : 1as CIP antibiotic solution is added dropwise to aqueous solutions of LN2 : 1.

A pronounced linear correlation was obtained at lower concentrations of CIP antibiotics, with a correlation coefficient (R^2) of 0.9906 and a Stern–Volmer quenching constant (K_{SV}) of 3.57×10^4 M^{-1} (Fig. 11a). The limit of detection (LOD) for CPF was calculated from the slope of the calibration curve and the standard deviation of the blank measurements, yielding a value of 0.982 ppm (Fig. 11b). To further evaluate the reliability of LN2 : 1 as a sensing platform, anti-interference studies were conducted. These investigations revealed that the fluorescence quenching response of LN2 : 1 toward CIP remained stable and reproducible in aqueous media, even when other antibiotics of comparable concentrations were present. The negligible influence of competing antibiotics on the sensing process confirms that the interaction between LN2 : 1 and CIP is highly specific. Consequently, LN2 : 1 demonstrates excellent selectivity and robustness, establishing its capability to accurately identify CIP in complex environments containing multiple potential interferents (Fig. 12). Fig. 12 illustrates the fluorescence response of various antibiotics in the absence and presence of CIP, highlighting that CIP induces a significantly stronger quenching effect even in a competitive multi-antibiotic environment. This behaviour confirms the selective recognition of CIP by LN2 : 1 and demonstrates that the sensing response toward CIP remains dominant and distinguishable in the presence of potential interfering antibiotics, underscoring the robustness of the sensing platform for complex sample matrices.

6.2.3. Recyclability and reusability of LN2 : 1. The advantage of a highly luminescent sensor lies in its potential for diverse applications as a sensing material. To assess the recyclability of LN2 : 1, fluorescence-based detection of CIP antibiotics was carried out in ethanolic medium. After each sensing experiment, the dispersed LN2 : 1 was recovered by repeated centrifugation with H_2O to effectively remove residual CIP molecules. The post-sensing photoluminescence spectra

Open Access Article. Published on 08 April 2026. Downloaded on 4/8/2026 8:29:56 PM.
This article is licensed under a Creative Commons Attribution-NonCommercial 3.0 Unported Licence.

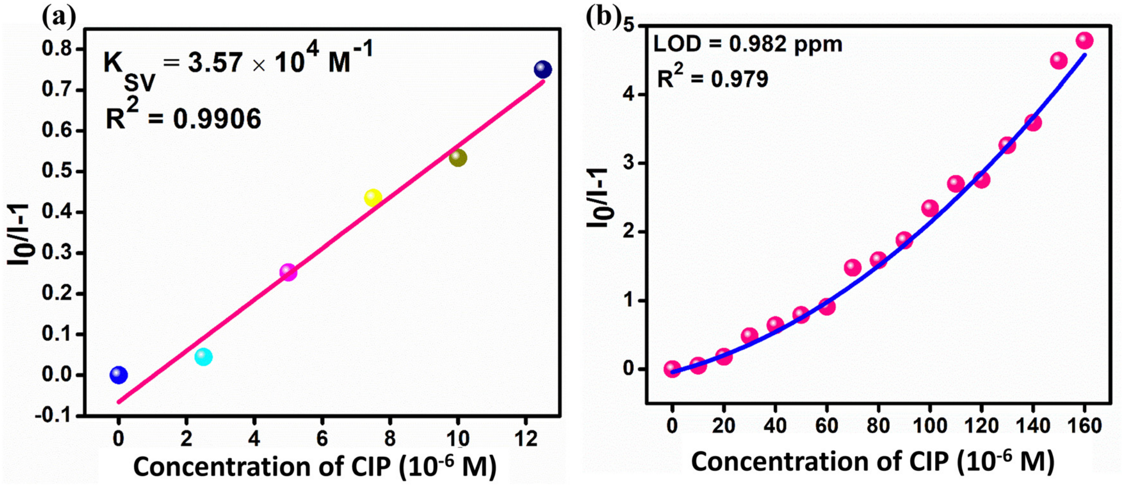

Fig. 11 (a) Linear S–V curve of LN2 : 1 at low concentrations of CIP antibiotic solution. (b) S–V plot of LN2 : 1 dispersed in methanolic medium with gradual addition of CIP antibiotic solution.

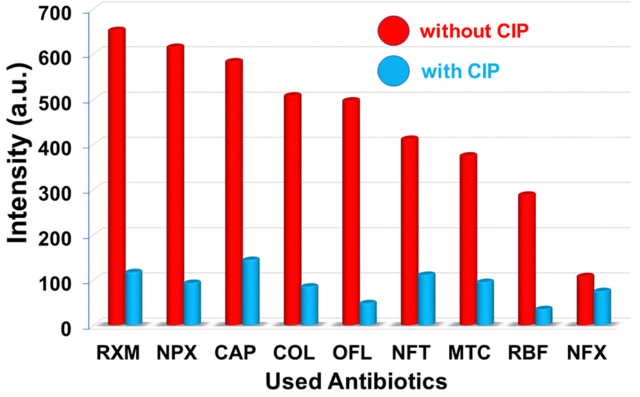

Fig. 12 Fluorescence intensity of antibiotics with and without CIP antibiotics.

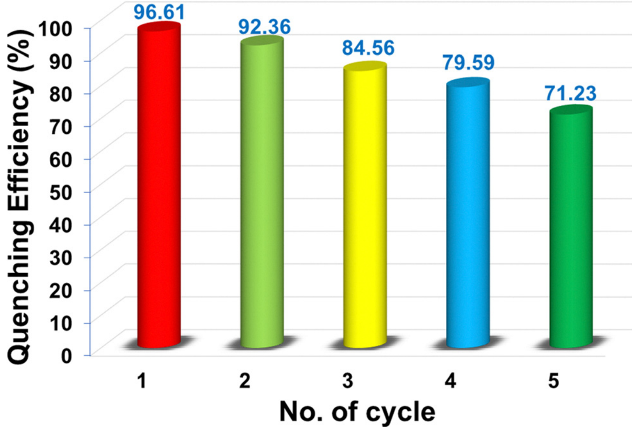

Fig. 13 The quenching efficiency of LN2 : 1 after five cycles.

revealed negligible variations in emission intensity, with only a slight reduction observed after five consecutive cycles. This minor decrease can be attributed to partial energy transfer and the presence of residual ions on the material's surface.[136–138] Importantly, the material consistently retained its quenching efficiency throughout all cycles (Fig. 13). The recyclability of LN2 : 1 can be ascribed to weak ion-channel interactions and competitive absorption processes, which ensure that the framework remains structurally and functionally stable during repeated use. Collectively, these findings highlight LN2 : 1 as a robust, reusable, and highly efficient luminescent probe for the sensitive detection of CIP antibiotics in aqueous media.

6.2.4. Mechanism behind fluorescence detection. Previous investigations have linked luminescent material recognition of antibiotics to processes like partial framework breakdown, coordination complex ion exchange, and competitive analyte adsorption or binding. Here, fluorescence quenching behaviour was examined to clarify the LN2 : 1 sensing mechanism toward CIP antibiotics. The quenching likely stems from electron transfer with CIP, diminishing energy transfer between π and π* orbitals in nitrogen-rich ligands of LN2 : 1. Resonance energy transfer (RET) contributes significantly as well, governed by spectral overlap between the UV-Vis absorption spectrum of CIP and the excitation spectrum of LN2 : 1. As shown in Fig. 14, the substantial overlap between the absorption spectrum of CIP and the excitation spectrum of LN2 : 1 confirms the major role of RET in the quenching effect.

The UV–Vis absorption spectrum of CIP antibiotics displays a significantly greater overlap with the excitation spectrum of LN2 : 1 compared to other analytes, which is consistent with sensing mechanisms reported in previous studies.[139–141] This pronounced spectral overlap facilitates the efficient quenching of LN2 : 1 fluorescence by CIP, accounting for the higher quenching efficiency observed. The underlying mechanism can be attributed to the competitive absorption of excitation energy by CIP molecules, which effectively compete with LN2 : 1 for the same excitation wavelength energy. Consequently, the available excitation energy for the materials is reduced, leading

Open Access Article. Published on 08 April 2026. Downloaded on 4/8/2026 8:29:56 PM.
This article is licensed under a Creative Commons Attribution-NonCommercial 3.0 Unported Licence.

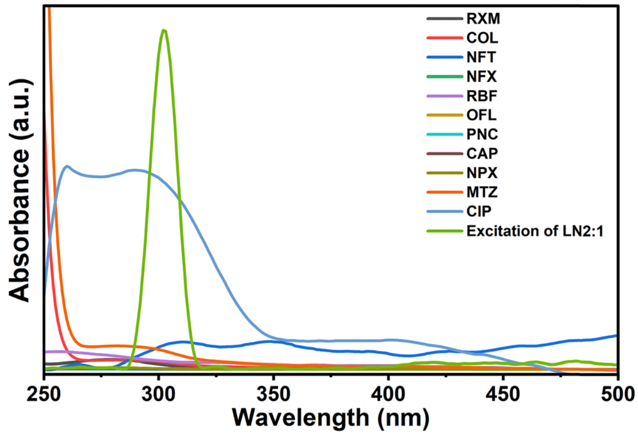

Fig. 14 Spectral overlap between the UV-Vis absorption spectra of various analytes and the excitation spectra of LN2 : 1.

to diminished fluorescence emission. These results clearly establish that the quenching process is predominantly governed by competitive absorption and electron-transfer transitions, rather than by structural decomposition or degradation of the LN2 : 1 framework (Table 4).

6.3. Photocatalytic degradation of Cresol Red

A highly effective photocatalyst should be able to degrade organic pollutants (REDOX) in addition to photo-reducing them. The model pollutant used in the investigation for photocatalytic reduction in Cresol Red. Fig. 15a and b illustrate how the synthesized catalyst's photocatalytic performance in lowering CR in the presence of sunlight was assessed. The CR dye was exposed to light for 120 minutes after undergoing a 30-minute dark reaction to achieve adsorption–desorption equilibrium with the catalysts. Following the arrangement, the photocatalytic degradation efficiency was LN2 : 1 > LN1 : 1 > LN1 : 2 > Co–Al LDH > g-C_3N_5. The subsequent photodegradation of CR was made easier by the improved contact and adsorption of CR on the surface of g-C_3N_5, which was assisted by Co–Al LDH. As the amount of LDH increased, the photocatalytic activity improved and peaked at LN2 : 1. However, the performance somewhat declined beyond this composition, most likely as a result of the high bulk of g-C_3N_5, which most likely prevented efficient light interaction. For the remaining trials, the LN2 : 1 catalyst was chosen as the optimal catalyst.

The LN2 : 1 composite, which is negatively charged, demonstrated the maximum photodegradation of the CR dye at pH 5, according to studies on the effect of pH on the photodegradation process (Fig. 15c). There are a number of reasons behind this. Even though CR and the catalyst are negatively charged, the adsorption of CR may be aided by certain surface-active sites or functional groups on the composite that allow weak interactions like hydrogen bonds or van der Waals forces. Furthermore, at pH 5, a slight protonation of surface groups may lessen the total negative charge, improving the CR interaction environment. Additionally, even though the catalyst and CR are electrostatically repelled, the composite's capacity to effectively separate and transfer charge carriers at this pH improves the photodegradation process. The composite's stability at pH 5 guarantees that it will retain its catalytic effectiveness and structural integrity, which further enhances the photodegradation of CR.[150] A number of operational aspects need to be taken into account in order to maximize the reaction rate and improve photocatalytic performance. To the reaction medium, varying quantities of catalyst (from 0.02 to 0.1 g) were applied. As shown in Fig. 15d, the reduction rate improved significantly when the catalyst dosage was raised from 0.02 to 0.04 g, reaching 90.5% after 120 minutes. But after this dosage, the pace of reduction began to drop, most likely as a result of less light absorption. Aggregation occurred when the catalyst quantity increased further, resulting in less exposure to visible light and, as a result, poorer photocatalytic efficiency. As shown in Fig. 15e, the effect of CR concentration on the photocatalytic degradation pathway was also examined. At different time intervals (0, 30, 60, 90, and 120 minutes), the absorbance of CR was measured, and it ranged from 0.02 to 0.1 g L^{-1}. The absorbance peak at 434 nm, which is associated with CR, progressively declined over time, as shown in Fig. 15f. The maximum reduction efficiency, which held true for all concentrations, was attained after 120 minutes of exposure. Additionally, as Fig. 15g illustrates, the rate of decline over time followed pseudo-first-order kinetics. Eqn (3) and (4) of the first-order kinetics are clearly shown below.

Fig. 15h, where the degradation kinetics are shown as C_0/C_t *vs.* time, shows the interaction between the initial concentration of CR (C_0) and CR concentration at a certain time period (C_t). The degradation efficiency was assessed using the pseudo-first-order kinetics-corresponding apparent rate constant (K_{app}). According to the first-order kinetics model, the K_{app} value of LN2 : 1 was 0.016 min^{-1}, almost 2.66 times greater than that of

Table 4 Comparison of the limit of detection (LOD) values for ciprofloxacin (CIP) using LN2 : 1 and other previously reported sensing materials

Catalyst	Method	Analytes	LOD	Ref.
Cu-MOF	Electrochemical	CIP	3.29 μM	142
Dy-MOF	Fluorescent	CIP	0.27 μM	143
Cd-MOF	Fluorescent	CIP	1.70 μM	144
NH_2–UiO-66/RGO	Electrochemical	CIP	10.86 μA μM^{-1}	145
Co-MOFs	Electrochemical	CIP	0.017 μM	146
Au/C_3N_4/GN/GCE	Electrochemical	CIP	0.42 μmol L^{-1}	147
Eu^{3+}@GaMOF	Fluorescent	CIP	7.243 μM	148
Eu MOFs	Fluorescent	CIP	0.050 μM	149
LN2 : 1	Fluorescent	CIP	2.96 μM (0.982 ppm)	This work

Open Access Article. Published on 08 April 2026. Downloaded on 4/8/2026 8:29:56 PM.
This article is licensed under a Creative Commons Attribution-NonCommercial 3.0 Unported Licence.

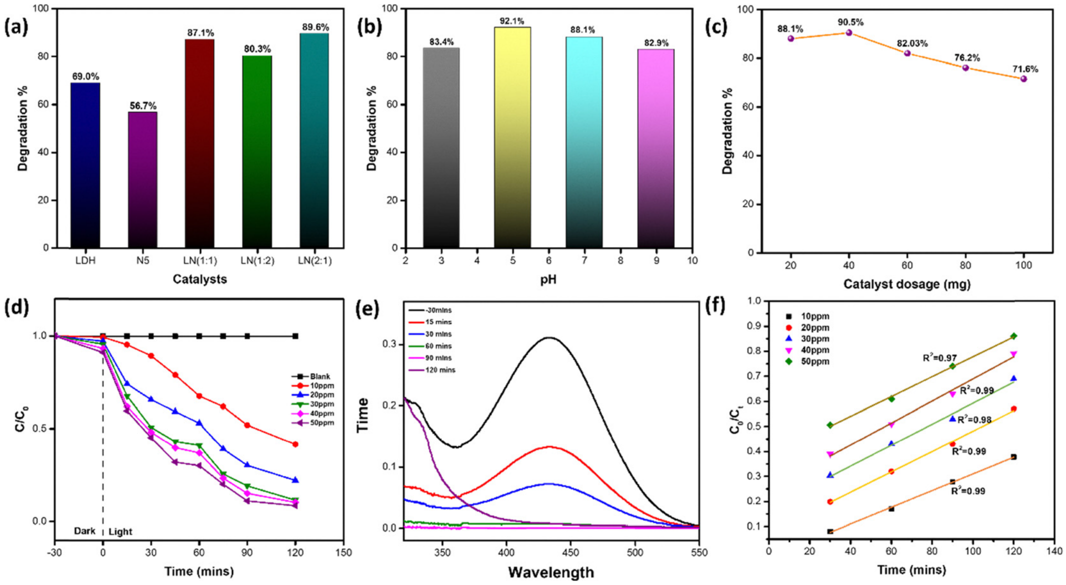

Fig. 15 (a) Effect of various catalysts, (b) effect of solution pH (3, 5, 7, and 9), (c) effect of catalyst dosage (10 mg, 20 mg, 30 mg, 40 mg, and 50 mg), (d) effect of solution concentration (10–50 ppm) with different time intervals (every 30-minute interval), (e) absorbance with time, and (f) photocatalytic degradation kinetics of CR of various concentrations with time by the LN2 : 1 catalyst.

Table 5 Rate constant (in min^{-1}) and regression coefficient (R^2) for various concentrations of CR obtained from the kinetic study, suggesting pseudo-first-order kinetics

Cresol Red dye concentration (ppm)	Time (min)	K_{app} (min^{-1})	Regression coefficient (R^2)
10	120	0.016	0.99
20	120	0.180	0.99
30	120	0.209	0.98
40	120	0.243	0.99
50	120	0.336	0.97

pristine Co–Al LDH (0.006 min^{-1}) and 1.7 times more than that of pristine g-C_3N_5 (0.009 min^{-1}). Additionally, with the change in CR concentration, the degradation rate reduces at higher concentrations, as shown by the K_{app} value decreasing with a rise in initial CR concentration. Table 5 provides a summary of these patterns. Furthermore, Fig. 15i illustrates the LN2 : 1 photocatalyst's capacity to decrease CR during four cycles, confirming its possible stability and reusability.

6.4. Photocatalytic hydrogen peroxide production

Apart from photocatalytic degradation of antibiotics and dyes, the adaptability of the catalyst was evaluated by its performance in the oxygen reduction process. The ability of the catalyst to produce hydrogen peroxide (H_2O_2) by photocatalysis was assessed when exposed to visible light (λ > 420 nm). The catalyst was first added to ultrapure water and subjected to 10-minute ultrasonication. To attain adsorption–desorption equilibrium, the sample was agitated in a quartz reactor without light for half an hour before being exposed to light. Following that, the sample was exposed to light for 120 minutes, both with and without oxygen bubbling during the reaction, as shown in Fig. 16a. An external oxygen supply is crucial for the oxygen reduction reaction and must be sufficiently provided to the solution, as demonstrated by the variation in H_2O_2 production shown in Fig. 16b. To delve deeper, the rate of H_2O_2 formation was evaluated after adding various sacrificial agents (electron donors) to the sample solution at a volume ratio of 10% V/V. Among ethanol, methanol, and 2-propanol, 2-propanol proved to be the most effective electron donor, as illustrated in Fig. 16c. Similar experiments were conducted on all catalysts, with the results displayed in Fig. 16a revealing that LN2 : 1 generated the highest amount of H_2O_2 (1903.28 μM L^{-1}), which is 16.43-fold greater than that generated by pristine Co–Al LDH (115.83 μM L^{-1}) and 5.5-fold higher than that by the pure g-C_3N_5 (340.5 μM L^{-1}). The absorbance peaks observed at 280 nm and 350 nm (see Fig. 16d) correspond to H_2O_2 concentration, with maximal generation recorded at 120 minutes. Possible interactions among produced H_2O_2 molecules could result in self-decomposition; hence, understanding the kinetics of H_2O_2 formation and degradation is vital during photocatalytic studies. A comprehensive grasp of these dynamics is necessary to fully elucidate the photocatalytic H_2O_2 production process. The reaction kinetics model for H_2O_2 formation is represented by eqn (5).

$$[H_2O_2] = \frac{K_f}{K_d}[1 - \exp(-K_d \times t)] \tag{5}$$

Notably, both first-order and zeroth-order kinetics are observed here. According to the graph shown in Fig. 16f, LN2 : 1 had the greatest K_f (rate of formation) values of any catalyst, although other catalysts had noticeably low K_d (rate of dissociation) values. These results are consistent with the formation of a heterojunction, which efficiently increases H_2O_2 production. Furthermore, Fig. 16e illustrates the LN2 : 1 photocatalyst's capacity to produce H_2O_2 throughout three cycles, confirming its possible stability and reusability (Table 6).

Open Access Article. Published on 08 April 2026. Downloaded on 4/8/2026 8:29:56 PM.
This article is licensed under a Creative Commons Attribution-NonCommercial 3.0 Unported Licence.

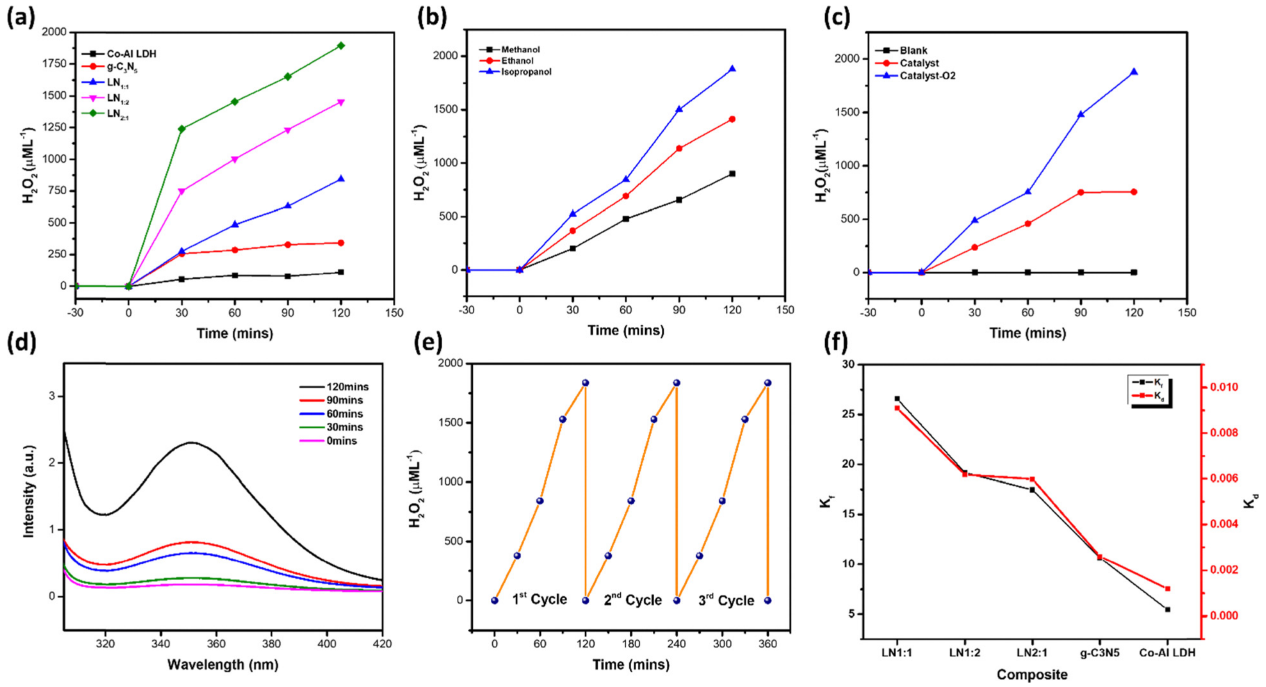

Fig. 16 (a) Effect of various catalysts, (b) effect of O_2 purging, (c) effect of sacrificial agents, (d) kinetics study, (e) absorbance peaks for H_2O_2 concentration with time, and (f) photocatalytic reusability of the LN2 : 1 catalyst.

Table 6 Rate of formation (K_f) values of LN1 : 1, LN2 : 1, LN1 : 2, Co–Al LDH and g-C_3N_5

Catalyst	Rate of formation (K_f)	Rate of dissociation (K_d)
LN1 : 1	26	0.009
LN1 : 2	21	0.007
LN2 : 1	17	0.005
g-C_3N_5	15	0.004
Co–Al LDH	10	0.002

6.5. Scavenging test and photocatalytic mechanism

The production and involvement of active reactive species are responsible for the effectiveness of photocatalytic reactions. A detailed scavenging study was conducted under known optimum reaction conditions to fully examine the mechanistic pathways involved in the photodegradation of ciprofloxacin (CIP) using the LN2 : 1 catalyst, as shown in Fig. 17. This method involved the introduction of specialised chemical scavengers to specifically intercept and neutralise specific active species that were expected to be involved in the photocatalytic system. At a regulated concentration of 1 mM, each of the four different scavengers, parabenzoquinone (PBQ), dimethyl sulfoxide (DMSO), isopropanol (IPA), and citric acid (CA), was added separately to the reaction mixture. The compounds were chosen based on their known affinity for particular reactive intermediates: CA for valence band holes (h^+), DMSO for photogenerated electrons (e^-), IPA for hydroxyl radicals (OH^-), and PBQ for superoxide radicals ($^\bullet O_2^-$).

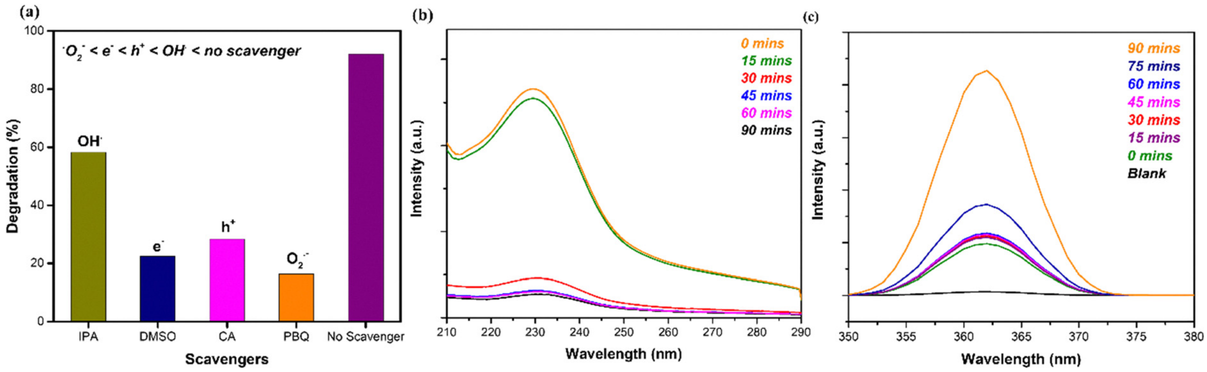

Fig. 17 (a) Effect of scavengers in the photodegradation of CIP by the LN2 : 1 catalyst, (b) NBT-UV analysis for superoxide detection, and (c) TA-PL analysis for hydroxyl radical detection.

The relative significance of each reactive species in the photocatalytic process was deduced by methodically tracking the degradation efficiency of CIP in the presence of various scavengers. According to the experimental results, the addition of

Open Access Article. Published on 08 April 2026. Downloaded on 4/8/2026 8:29:56 PM.
This article is licensed under a Creative Commons Attribution-NonCommercial 3.0 Unported Licence.

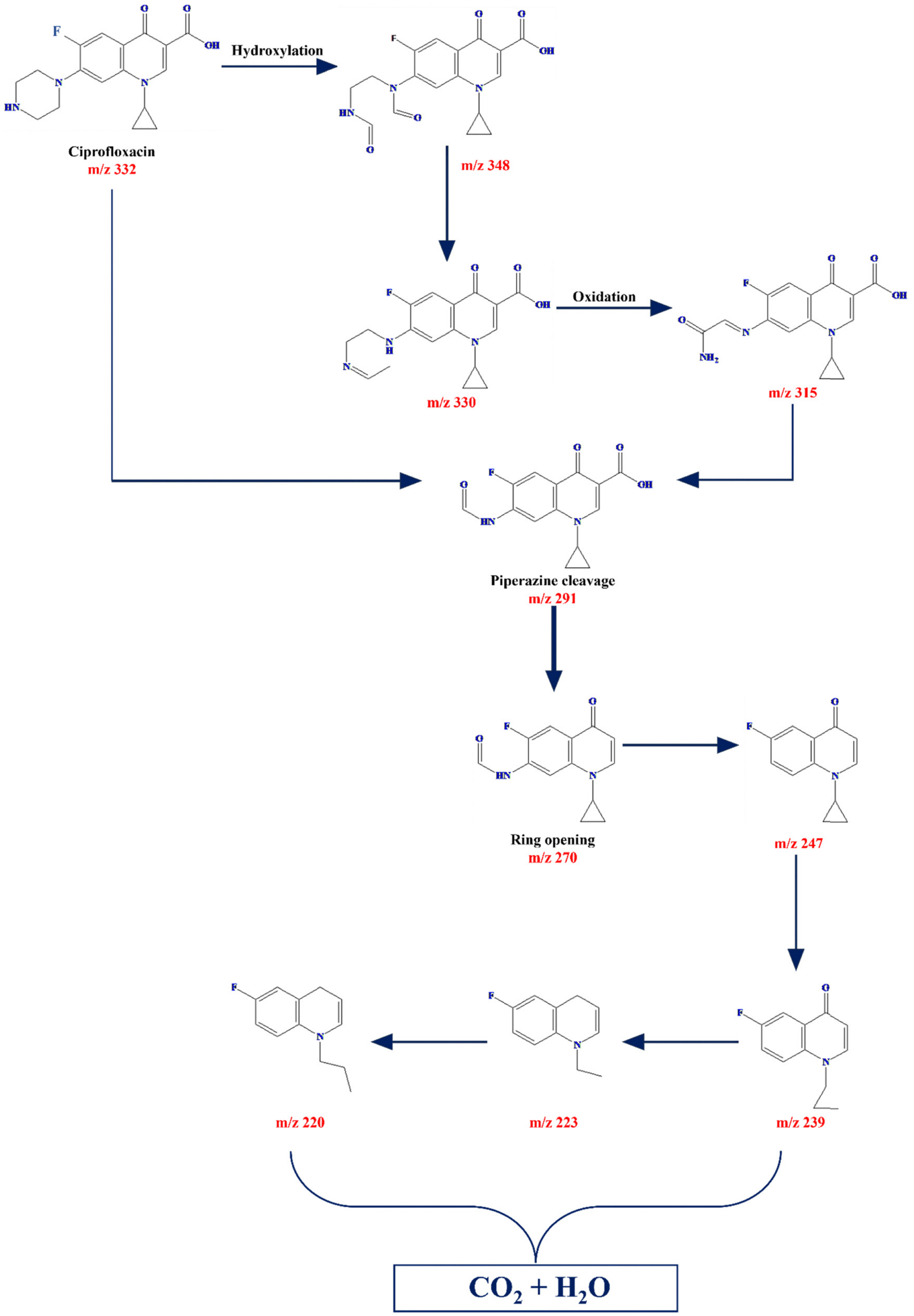

Scheme 2 Proposed photocatalytic degradation pathway of ciprofloxacin over LN2 : 1 under visible light irradiation.

Open Access Article. Published on 08 April 2026. Downloaded on 4/8/2026 8:29:56 PM.
This article is licensed under a Creative Commons Attribution-NonCommercial 3.0 Unported Licence.

DMSO and CA significantly inhibited the degradation of CIP, with efficiencies falling to 22.2% and 28.4%, respectively. This strong suppression implies that photogenerated electrons and holes play important roles in the total photocatalytic activity. However, a preserved efficiency of 58.6% indicates that the introduction of IPA, which targets hydroxyl radicals, had a relatively small effect. This finding suggests that, in the investigated settings, hydroxyl radicals have a less significant impact. The significance of hole-mediated oxidation pathways was highlighted by the significant decrease in photocatalytic effectiveness (to 44.4%) that resulted from the addition of citric acid, which is known to scavenge valence band holes. All these findings show that electrons, superoxide radicals, and holes work together to drive the photocatalytic degradation of ciprofloxacin by the LN2 : 1 catalyst, with hydroxyl radicals playing a comparatively little role. To increase the effectiveness of pollutant removal, photocatalytic devices and reaction conditions may be optimised with the help of this mechanistic knowledge.

Two complementary probe techniques were used to investigate the production of reaction oxygen species (ROS) during photocatalysis. Due to its sensitivity to superoxide radicals, the nitro blue tetrazolium (NBT) method is frequently used to detect superoxide radicals. NBT is reduced and its distinctive absorbance drops when superoxide radicals are present, allowing for a quantitative evaluation. This work used UV-vis spectroscopy to measure the absorbance of a suspension containing 0.02 g of LN2 : 1 photocatalyst in 20 mL of 50 mM phosphate buffer with 0.2 mM NBT, which was exposed to sunlight at certain intervals. The strength of the absorption peak at 260 nm gradually dropped after 60 minutes in comparison to the blank, as shown in Fig. 17b, displaying ongoing superoxide species

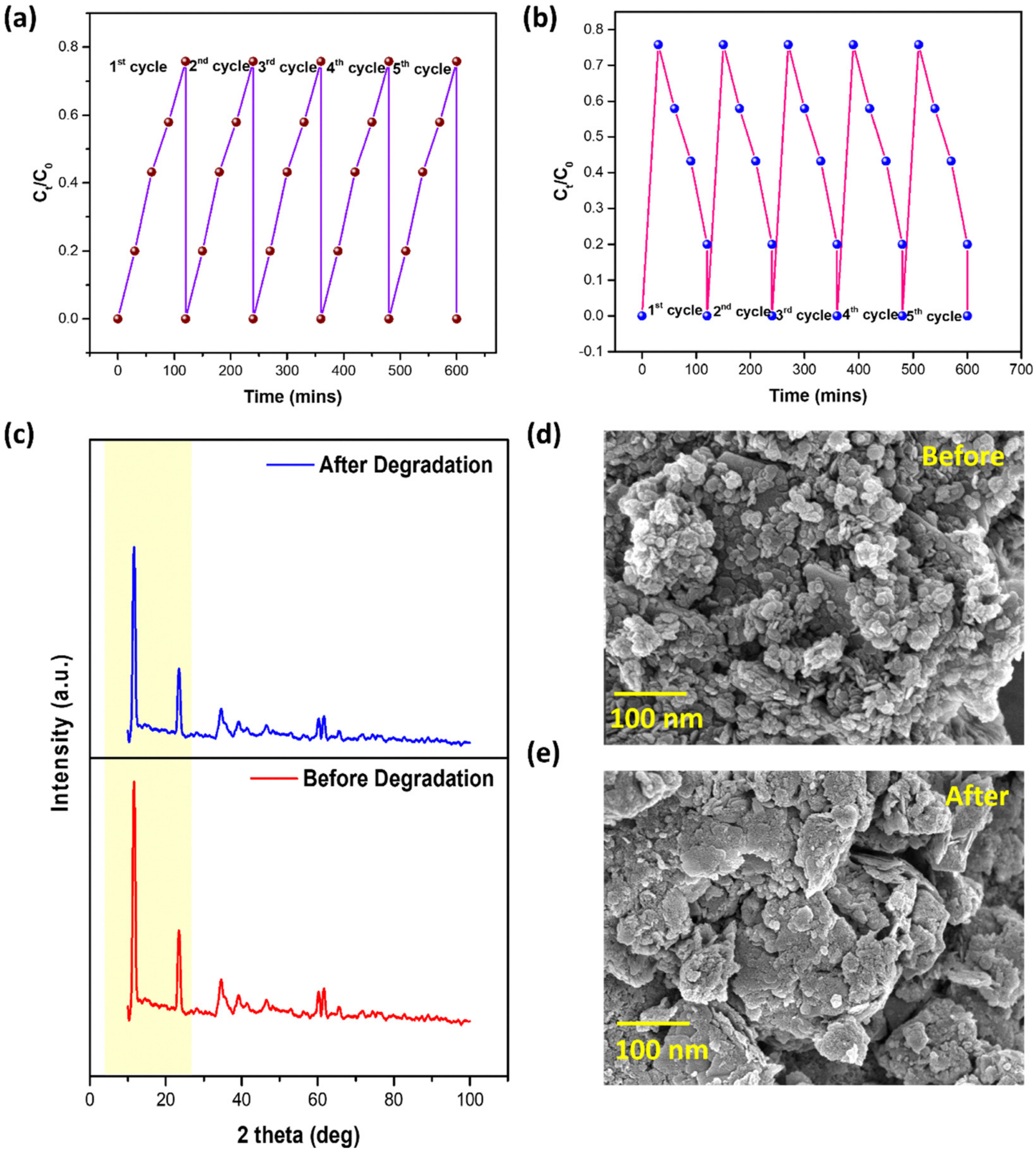

Fig. 18 (a) Reusability test for CIP, (b) reusability test for CR, (c) XRD analysis, and (d), (e) FE-SEM images before and after photocatalysis.

Open Access Article. Published on 08 April 2026. Downloaded on 4/8/2026 8:29:56 PM.
This article is licensed under a Creative Commons Attribution-NonCommercial 3.0 Unported Licence.

generation. The terephthalic acid photoluminescence (TA-PL) method was used to further explore the production of hydroxyl radicals. Terephthalic acid preferentially interacts with hydroxyl radicals in this reaction to produce 2-hydroxyterephthalic acid (TAOH), which fluoresces at about 426 nm when excited at 315 nm. 0.02 g of photocatalyst was dissolved in 20 mL of a 0.4 M NaOH solution for the measurements, and the solution was then exposed to sunlight for varying amounts of time. The fluorescence intensity increased gradually with irradiation duration, as shown in Fig. 17c, indicating an effective production of hydroxyl radicals under the specified circumstances. Both the reaction mechanisms are well established in eqn (6) and (7).

$$\text{NBT} + {}^{\bullet}\text{O}_2{}^{-} \rightarrow \text{Formazan} \quad \text{(reduced product)} \qquad (6)$$

$$\text{TA} + {}^{\bullet}\text{OH} \rightarrow \text{TAOH} \quad \text{(fluorescent product)} \qquad (7)$$

The Co–Al LDH/g-C_3N_5 heterostructure's strategic design combines the complementary optical characteristics of both components, greatly expanding the overall light absorption spectrum. Because of its appropriate bandgap, Co–Al LDH mostly absorbs higher energy photons, but g-C_3N_5 efficiently captures lower energy visible light to increase the photoresponsive effect of the composite. Superior photocatalytic performance is the final result of this synergistic interaction, which also improves light gathering and encourages effective charge carrier formation. Strong interfacial contact is made possible by the interaction between Co–Al LDH and g-C_3N_5, which is necessary for quick and effective charge transfer across the heterojunction.

6.6. Photodegradation pathway of CIP

LC-MS analysis was carried out to identify the intermediate species obtained during the photocatalytic CIP degradation (CIP) over the LN2 : 1 photocatalyst under visible light irradiation, and the detailed pathway is depicted in Scheme 2. In this instance, the photogenerated active species and CIP molecules interacted to produce degradation products. After 60 min, the parent ion at *m/z* 332.05 ($[M + H]^+$) was still prominent, accompanied by multiple intermediate species at *m/z* 373.10, 370, 287, 270, 247.1, 242.9, 229.1, 223.05, and 204.75.[151] The peaks at *m/z* 373 and 370 were attributed to hydroxylated/oxidized derivatives formed *via* reactive oxygen species (${}^{\bullet}$OH) attack.[152] The fragment at *m/z* 287 suggests decarboxylation of CIP, while *m/z* 270 and 274 indicate piperazine ring cleavage and progressive fragmentation of the quinoline core.[153] At 120 min irradiation, a notable decrease in higher-mass oxidized intermediates (*e.g.*, *m/z* 373 and 365) was observed, accompanied by an increase in lower molecular weight fragments, particularly *m/z* 223.05 (as shown in Fig.S5), which became the dominant intermediate.[154] The persistence of *m/z* 270 suggests ongoing nitrogen-containing ring degradation, while the shift toward smaller fragments confirms advanced quinolone ring opening and oxidative breakdown.[153] The time-dependent transformation from hydroxylated derivatives to low-molecular-weight fragments demonstrates a stepwise ROS-mediated degradation pathway, ultimately progressing toward mineralization. The LCMS findings were further supported by HPLC analysis. The pure CIP exhibited a sharp peak at a retention time (R_t) of 0.993 min. After 60 min of visible light irradiation, R_t shifted to 1.094 min, indicating the formation of intermediate degradation products with altered polarity. Upon 120 min irradiation, R_t slightly decreased to 1.048 min,

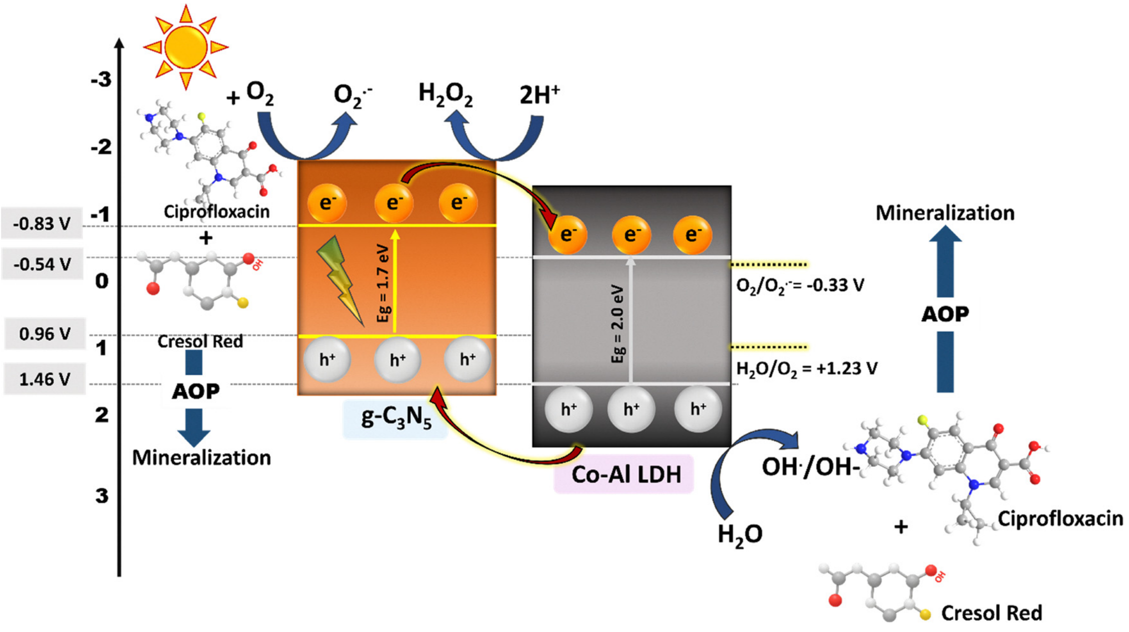

Scheme 3 Plausible mechanism.

Open Access Article. Published on 08 April 2026. Downloaded on 4/8/2026 8:29:56 PM. This article is licensed under a Creative Commons Attribution-NonCommercial 3.0 Unported Licence.

suggesting further transformation into smaller and relatively more polar fragments.[155] The gradual shift and modification of retention times corroborate the LC-MS results, confirming the time-dependent structural transformation and progressive oxidative degradation of CIP.

6.7. Reusability test

The stability and recyclability of the LN2 : 1 photocatalyst were evaluated through repeated degradation of ciprofloxacin (CIP) (Fig. 18a) and Cresol Red (CR) (Fig. 18b) over at least 5 cycles, and the results strongly confirm its robustness. The recyclability studies show that the degradation efficiency remains consistently high across multiple runs for both pollutants, with only a slight decline after the 5 successive cycles, which is mainly due to minor material loss or surface fouling during recovery. Structural analysis using XRD and FTIR studies (as shown in Fig. 18c) further supports its stability, as the diffraction patterns recorded before and after the reactions exhibit identical yet a slight shift in the peak positions without the emergence of any new phases, indicating that the crystal structure of LN2 : 1 remains intact throughout the photocatalytic process. Correspondingly, FESEM images (see Fig. 18d and e) reveal that the nanoscale morphology of the catalyst is largely preserved even after repeated use. The aggregated and textured surface of the fresh sample shows no significant deformation post-reaction, aside from minimal smoothing or particle fusion that commonly occurs under extended irradiation and stirring. Together, the reusability performance, unaltered crystallinity, and preserved surface architecture confirm that LN2 : 1 maintains excellent physicochemical and morphological integrity, making it a highly durable and efficient photocatalyst suitable for real-world applications (Scheme 3).

7. Conclusion

The present work highlights the successful development of a Co–Al LDH/g-C_3N_5 nanocomposite as a highly efficient visible light-driven photocatalyst for the degradation of organic and dye-based pollutants. The composite exhibited remarkable performance in degrading ciprofloxacin and Cresol Red dye within 120 minutes, accompanied by the simultaneous production of a significant amount of H_2O_2, which acted as an auxiliary oxidising agent to boost the photocatalytic pathway. The synergistic interaction between Co–Al LDH and g-C_3N_5 resulted in enhanced light absorption, efficient charge carrier separation, and prolonged lifetime of photogenerated electrons and holes, thereby intensifying the generation of reactive oxygen species (ROS) such as $^{\bullet}OH$ and $O_2^{\bullet-}$ radicals. These factors collectively promoted rapid pollutant degradation and effective mineralisation. Beyond pollutant removal, the system demonstrates a sustainable and green approach, as it harnesses visible light and generates H_2O_2 *in situ*, reducing the dependence on external oxidants. Thus, this study not only validates the practical applicability of the Co–Al LDH/g-C_3N_5 nanocomposite for wastewater treatment but also opens new avenues for designing multi-functional photocatalysts that integrate pollutant degradation with self-sustained oxidant production, offering a viable strategy for addressing complex environmental challenges.

Author contributions

Alaka Rath: conceptualisation, visualisation, writing – original draft, investigation, resources, formal analysis. Pratyush Kumar Sahu: investigation, resources, formal analysis. Vibhav Shukla: resources, formal analysis. Aslisha Champati: investigation, formal analysis. Kafeel Ahmad Siddiqui: visualisation, formal analysis. Brundabana Naik: conceptualisation, visualisation, supervision, writing – review & editing.

Conflicts of interest

There are no conflicts of interest to declare.

Abbreviations

LN	Co–Al LDH/g-C_3N_5
PBQ	*p*-benzoquinone
IPA	Isopropanol
CA	Citric acid
DMSO	Dimethyl sulfoxide
CIP	Ciprofloxacin
CAP	Chloramphenicol
NFX	Norfloxacin
NFT	Nitrofurantoin
NPX	Naproxen
MTX	Metronidazole
RXM	Roxithromycin
COL	Colchine
RBF	Riboflavin
CR	Cresol Red

Data availability

All data generated or analyzed during the study are included in the manuscript. There are no data generated or analyzed during the study from other resources.

Supplementary information (SI) is available. Fig. S1 (a) Fluorescence intensity measurements of Co-Al LDH in different solvent solutions, and (b) Comparative quenching efficiencies of Co-Al LDH in solvent solution; Fig. S2 (a) Fluorescence intensity measurements of g-C_3N_5 in different solvent solutions; and (b) Comparative quenching efficiencies of g-C_3N_5 in solvent solution; Fig. S3 (a) Fluorescence intensity measurements of Co-Al LDH in different antibiotic solutions; and (b) Comparative quenching efficiencies of Co-Al LDH in solvent solution with specific antibiotics; Fig. S4 (a) Fluorescence intensity measurements of g-C_3N_5 in different antibiotic solutions; and (b) Comparative quenching efficiencies of g-C_3N_5 in solvent solution with specific antibiotics; Fig. S5 Tauc plots for

This journal is © The Royal Society of Chemistry and the Centre National de la Recherche Scientifique 2026

Open Access Article. Published on 08 April 2026. Downloaded on 4/8/2026 8:29:56 PM. This article is licensed under a Creative Commons Attribution-NonCommercial 3.0 Unported Licence.

bandgap estimation of (a) Co-Al LDH (b) LN1:1 (c) LN1:2 and (d) LN2:1; Fig. S6 LC-MS analysis of ciprofloxacin over LN2:1 composite after 120 mins of photodegradation. See DOI: https://doi.org/10.1039/d5nj04998a.

Acknowledgements

All the authors are thankful to the authority of Siksha 'O' Anusandhan, deemed to be a University in Odisha, India, and the National Institute of Technology (NIT), Raipur, for providing research facilities to carry out this work.

References

1 F. R. Ihsan, J. G. Bloomfield and L. V. Monrouxe, *Front. Med.*, 2024, **11**, 1465662.

2 A. Góralczyk-Bińkowska, A. Długoński, P. Bernat, J. Długoński and A. Jasińska, *Sci. Rep.*, 2021, **11**, 23829.

3 F. A. Akinsola, M. M. Ologundudu, M. O. Akinsola and N. M. Odhiambo, *Heliyon*, 2025, **14**, 1183.

4 R. M. Doherty, M. R. Heal, P. Wilkinson, S. Pattenden, M. Vieno, B. Armstrong, R. Atkinson, Z. Chalabi, S. Kovats and A. Milojevic, *et al.*, *Environ. Heal.*, 2009, **8**, S8.

5 J. N. Nehul, *Environ. Rep.*, 1981, 34–39.

6 D. W. Moore, B. Ruffle, A. McQueen, S. Thakali and D. Edwards, *Integr. Environ. Assess. Manag.*, 2023, **19**, 1192–1206.

7 J. Munthe, E. Brorström-Lundén, M. Rahmberg, L. Posthuma, R. Altenburger, W. Brack, D. Bunke, G. Engelen, B. M. Gawlik and J. van Gils, *et al.*, *Environ. Sci. Eur.*, 2017, **29**, 13.

8 K. Kotyal, *Environ. Rep.*, 2023, **5**, 1–5.

9 N. Goodarzi, Z. Ashrafi-Peyman, E. Khani and A. Z. Moshfegh, *Catalysts*, 2023, **13**, 1102.

10 M. A. Ahmed and A. A. Mohamed, *RSC Adv.*, 2023, **13**, 421–439.

11 M. A. Ahmed, S. A. Mahmoud and A. A. Mohamed, *RSC Adv.*, 2024, **14**, 25629–25662.

12 C. G. Olorunnisola, D. Olorunnisola, C. Neumann, W. Koopman, C. Günter, H. Seitz, H. M. Rawel, E. I. Unuabonah and A. Taubert, *ACS omega*, 2025, **10**, 41395–41412.

13 M. A. Ahmed, S. A. Mahmoud and A. A. Mohamed, *RSC Adv.*, 2025, **15**, 15561–15603.

14 O. P. Onotu, H. S. Samuel, D. A. Undie, O. O. Akinpelu, F. A. Ibekwe and E. E. Etim, *Discov. Nano*, 2025, **20**, 1–33.

15 K. H. H. Aziz, F. S. Mustafa, M. A. H. Karim and S. Hama, *Mater. Adv.*, 2025, **6**, 3433–3454.

16 A. Adenaya, F. Zumbika, R. Rios-Quintero, P. A. Lara-Martin, O. Wurl, M. Ribas Ribas, A. Hamprecht and T. Brinkhoff, *Front. Microbiol.*, 2025, **16**, 1624041.

17 T. Liu, W. Liu, X. Li, H. Wang, Y. Lan, S. Zhang, Y. Wang and H. Liu, *Sci. Rep.*, 2024, **14**, 19831.

18 H. Zhang, H. Quan, S. Yin, L. Sun and H. Lu, *Environ. Sci. Technol.*, 2022, **56**, 15941–15952.

19 Q. Yang, Y. Gao, J. Ke, P. L. Show, Y. Ge, Y. Liu, R. Guo and J. Chen, *Bioengineered*, 2021, **12**, 7376–7416.

20 H.-M. Zhao, H.-B. Huang, Z.-X. Zhan, Y.-Y. Ye, J.-L. Cheng, L. Xiang, Y.-W. Li, Q.-Y. Cai, Y. Xie and C.-H. Mo, *Sci. Total Environ.*, 2024, **912**, 169392.

21 M. A. Al Masud, S. Annamalai and W. S. Shin, *Chem. Eng. J.*, 2023, **465**, 142908.

22 B. Zhu, D. Song, T. Jia, W. Sun, D. Wang, L. Wang, J. Guo, L. Jin, L. Zhang and H. Tao, *ACS Omega*, 2021, **6**, 1647–1656.

23 M. Idrees, Z. U. H. Khan, S. Sabahat, J. Sun, N. S. Shah and J. Iqbal, *J. Mol. Liq.*, 2025, **424**, 127115.

24 C. Liu, H. Yu, W. Xiao, C. Gu, J. Yu, J. Li, J. Song, Y. Song, T. Sun and Z. Zou, *et al.*, *Appl. Surf. Sci.*, 2025, **682**, 161717.

25 X. Jin, X. Liu, Y. Li, T. Zhang, W. Ni, Z. Lu and C. Dong, *Cott. Blends*, 2024, **280**(Part 2), 135878.

26 D. Yang, F. Meng, Z. Zhang and X. Liu, *ACS Omega*, 2023, **8**, 21823–21829.

27 C. Liu, W. Xiao, X. Liu, Q. Wang, J. Hu, S. Zhang, J. Xu, Q. Zhang and Z. Zou, *J. Mater. Sci. Technol.*, 2023, **161**, 123–135.

28 H. Chi, P. Cao, Q. Shi, C. Song, Y. Lv and T. Peng, *Nanomaterials*, 2025, **15**, 383.

29 C. Liu, H. Yu, J. Li, X. Yu, Z. Yu, Y. Song, F. Zhang, Q. Zhang and Z. Zou, *Acta Phys.-Chim. Sin.*, 2025, **41**, 100075.

30 N. Jahan, M. A. Sayem, S. M. Maruf, R. Sultana and M. A. Bhuiyan, *AIP Adv.*, 2025, **15**, 105106.

31 T. Hayri-Senel, E. Kahraman, S. Sezer, N. Erdol-Aydin and G. Nasun-Saygili, *Heliyon*, 2024, **10**, e25433.

32 Y. Nosaka and A. Y. Nosaka, *Chem. Rev.*, 2017, **117**, 11302–11336.

33 X. Fan, Q. Fu, G. Liu, H. Jia, X. Dong, Y.-F. Li and S. Cui, *Environ. Sci. Ecotechnol.*, 2024, **22**, 100469.

34 S. R. D. Gamelas, J. P. C. Tomé, A. C. Tomé and L. M. O. Lourenço, *RSC Adv.*, 2023, **13**, 33957–33993.

35 C. Zhang, Y. Wu, D. Li and H.-L. Jiang, *Chem. Sci.*, 2025, **16**, 13149–13172.

36 S. Li, L. Shi, Y. Guo, J. Wang, D. Liu and S. Zhao, *Chem. Sci.*, 2024, **15**, 11188–11228.

37 A. R. Groves, UCL (University College London), 2021.

38 Q. Chen, *Chem. Eng. Process. Process Intensif.*, 2008, **47**, 787–792.

39 A. Yu, S. Liu and Y. Yang, *Chem. Commun.*, 2024, **60**, 5232–5244.

40 Y. Pang, H. Xie, Y. Sun, M.-M. Titirici and G.-L. Chai, *J. Mater. Chem. A*, 2020, **8**, 24996–25016.

41 P. J. M. Cordeiro-Junior, J. Lobato Bajo, M. R. V. Lanza and M. A. Rodrigo Rodrigo, *Ind. Eng. Chem. Res.*, 2022, **61**, 10660–10669.

42 J. An, Y. Feng, Q. Zhao, X. Wang, J. Liu and N. Li, *Environ. Sci. Ecotechnol.*, 2022, **11**, 100170.

43 H. W. Kim, V. J. Bukas, H. Park, S. Park, K. M. Diederichsen, J. Lim, Y. H. Cho, J. Kim, W. Kim and T. H. Han, *et al.*, *ACS Catal.*, 2019, **10**, 852–863.

Open Access Article. Published on 08 April 2026. Downloaded on 4/8/2026 8:29:56 PM.
This article is licensed under a Creative Commons Attribution-NonCommercial 3.0 Unported Licence.

44 L. P. de Souza, I. M. G. de Souza, R. S. Souto, M. S. Kronka, B. Ramos, M. R. V. Lanza, J. L. de Paiva and A. C. S. C. Teixeira, *Ind. Eng. Chem. Res.*, 2024, **63**, 18053–18066.

45 Q. Zhao, J. An, X. Wang and N. Li, *Int. J. Hydrogen Energy*, 2021, **46**, 3204–3219.

46 S. Mavrikis, M. Göltz, S. C. Perry, F. Bogdan, P. K. Leung, S. Rosiwal, L. Wang and C. de Leon, *ACS Energy Lett.*, 2021, **6**, 2369–2377.

47 Z. Sang, Y. Qiao, R. Chen, L. Yin, F. Hou and J. Liang, *Nat. Commun.*, 2025, **16**, 4050.

48 G. Fan, F. Li, D. G. Evans and X. Duan, *Chem. Soc. Rev.*, 2014, **43**, 7040–7066.

49 A. M. Tucker-Quiñónez, B. F. Rivadeneira-Mendoza, M. L. Gorozabel-Mendoza, I. B. Pérez-Almeida, A. J. Garcia-Guerrero, A. A. Dueñas-Rivadeneira, K. K. Yadav, L. A. Zambrano-Intriago and J. M. Rodriguez-Diaz, *Energy Nexus*, 2025, 100399.

50 A. A. Altalhi, E. A. Mohamed and N. A. Negm, *Energy Adv.*, 2024, **3**, 2136–2151.

51 B. Balcomb, M. Singh and S. Singh.

52 S. Nagappan, A. Karmakar, R. Madhu, H. N. Dhandapani, S. S. Roy and S. Kundu, *Catal. Sci. Technol.*, 2023, **13**, 6377–6391.

53 P. Miao, J. Zhao, R. Shi, Z. Li, Y. Zhao, C. Zhou and T. Zhang, *ACS ES&T Eng.*, 2022, **2**, 1088–1102.

54 C. Li, H. Jing, Z. Wu and D. Jiang, *Nanomaterials*, 2022, **12**, 3525.

55 A. A. Khan, M. Tahir and N. Khan, *Appl. Phys. Rev.*, 2025, **12**, 011313.

56 M. C. Maridevaru, F. Al Marzouqi, M. Nagaveni, M. M. Kumari, M. V. Shankar, M. Khraisheh and R. Selvaraj, *Int. J. Hydrogen Energy*, 2025, **105**, 189–202.

57 A. Jedras, J. Matusik, E. Dhanaraman, Y.-P. Fu and G. Cempura, *Langmuir*, 2024, **40**, 18163–18175.

58 S. Rajendran and R. Vijayaraghavan, *RSC Adv.*, 2025, **15**, 24802–24814.

59 W. Shao, Q. Wang, C. Huang and D. Zhang, *Mater. Adv.*, 2022, **3**, 1816–1824.

60 X. Wang, Y. Tuo, Y. Zhou, D. Wang, S. Wang and J. Zhang, *Chem. Eng. J.*, 2021, **403**, 126297.

61 P. Bobde, R. K. Patel, D. Panchal, A. Sharma, A. K. Sharma, R. S. Dhodapkar and S. Pal, *Environ. Sci. Pollut. Res.*, 2021, **28**, 59551–59569.

62 Y. Song, K. Ji, H. Duan and M. Shao, *Exploration*, 2021, **1**, 20210050.

63 U. A. Mohanty, D. P. Sahoo, L. Paramanik and K. Parida, *Sustain. Energy Fuels*, 2023, **7**, 1145–1186.

64 P. K. Sahu, A. Champati, A. Pradhan, N. K. Sahoo and B. Naik, *J. Nanoparticle Res.*, 2024, **26**, 261.

65 M. Asif, M. Saeed, M. Zafar, U.-S. Amjad, A. Razzaq and W. Y. Kim, *Results Phys.*, 2022, **42**, 105997.

66 B. Debnath, S. M. Hossain, A. Sadhu, S. Singh, V. Polshettiwar and S. Ogale, *ACS Appl. Mater. Interfaces*, 2022, **14**, 37076–37087.

67 Z. L. M. Botello, M. Illescas, B. C. Barja, S. E. Collins, G. E. Narda and M. C. Bernini, *CrystEngComm.*, 2025, **27**, 4470–4487.

68 V. Shukla, G. Aalam, S. W. Ali, M. Ahamd, N. Haq and K. A. Siddiqui, *New J. Chem.*, 2025, **49**, 1648–1662.

69 F.-H. Zhao, Y.-S. Li, S.-Q. Li, X.-H. Wu, Y.-C. He and Z.-L. Li, *CrystEngComm*, 2025, **27**, 2223–2232.

70 H. Yoo, C. Park, S. Lee and J. Y. Kim, *CrystEngComm*, 2025, **27**, 5965–5970.

71 Y. Liu, J. L. Li, N. Zhang, Y. Zhao, Q. L. Guan, Y. H. Xing and F. Y. Bai, *CrystEngComm*, 2025, **27**, 1939–1949.

72 Y. Lin, W. Zhang, Y. Lv, Y. Zhao, H. Cui, J. Sun, X. Li, D. Zhou and Z. Su, *CrystEngComm*, 2025, **27**, 4351–4359.

73 M. Aleksandrzak, K. Sielicki and E. Mijowska, *RSC Adv.*, 2020, **10**, 4032–4039.

74 C. Wu, S. Xue, Z. Qin, M. Nazari, G. Yang, S. Yue, T. Tong, H. Ghasemi, F. C. R. Hernandez and S. Xue, *et al.*, *Appl. Catal. B Environ.*, 2021, **282**, 119557.

75 R. Chalasani, A. Gupta and S. Vasudevan, *Sci. Rep.*, 2013, **3**, 3498.

76 Q. Qin, Y. Hu, J. Wang, Y. Yang, T. Lei, Z. Cui, S. Guo and S. Qin, *Nanoscale Adv.*, 2023, **5**, 2873–2878.

77 I. Palinko, P. Sipos, O. Berkesi and G. Varga, *J. Phys. Chem. C*, 2022, **126**, 15254–15262.

78 Q. Hao, X. Niu, C. Nie, S. Hao, W. Zou, J. Ge, D. Chen and W. Yao, *Phys. Chem. Chem. Phys.*, 2016, **18**, 31410–31418.

79 J. Liu, S. Wang, C. Zhao and J. Zheng, *Nanomaterials*, 2023, **13**, 499.

80 T. S. Rad, E. S. Yazici, A. Khataee, E. Gengec and M. Kobya, *Ultrason. Sonochem.*, 2023, **95**, 106358.

81 R. Zhu, W. Yuan, J. Cheng and X. Qiu, *Sustain. Chem. Environ.*, 2024, **8**, 100169.

82 J. Zai, Y. Liu, X. Li, Z. Ma, R. Qi and X. Qian, *Nano-Micro Lett.*, 2017, **9**, 21.

83 K. K. Ramankutty, H. Yang, A. Baghdasaryan, J. Teyssier, V. P. Nicu and T. Buergi, *Phys. Chem. Chem. Phys.*, 2022, **24**, 13848–13859.

84 M. C. Richardson and P. S. Braterman, *J. Phys. Chem. C*, 2007, **111**, 4209–4215.

85 Y. Xia, R. Liang, M.-Q. Yang, S. Zhu and G. Yan, *Nanomaterials*, 2021, **11**, 2762.

86 F. N. Mukhtar, N. A. Kamal, S. N. M. Johari, N. A. M. S. Bhari and N. A. Tajuddin.

87 E. Jamshidi, S. Dalvand, F. Manteghi and S. M. Mousavi-Khoshdel, *IScience.*, 2025, **28**, 111672.

88 A. Rahman and R. V. S. Pullabhotla, *Bull. Chem. React. Eng. Catal.*, 2022, **17**, 163–193.

89 J. Dong, Y. Zhang, M. I. Hussain, W. Zhou, Y. Chen and L.-N. Wang, *Nanomaterials*, 2021, **12**, 121.

90 M. Bradley, F. Izzia and S. Nunn.

91 Y. Huang, X. Ma, X. Wang and X. Liang, *J. Mol. Struct.*, 2013, **1031**, 30–37.

92 T. Dhanasekaran, R. Manigandan, A. Padmanaban, R. Suresh, K. Giribabu and V. Narayanan, *Sci. Rep.*, 2019, **9**, 13250.

93 G. Li, G. Zeng, Z. Chen, J. Hong, X. Ji, Z. Lan, X. Tan, M. Li, X. Hu and C. Tang, *Nanomaterials*, 2022, **12**, 2701.

94 Z. Liu, L. Teng, L. Ma, Y. Liu, X. Zhang, J. Xue, M. Ikram, M. Ullah, L. Li and K. Shi, *RSC Adv.*, 2019, **9**, 21911–21921.

Open Access Article. Published on 08 April 2026. Downloaded on 4/8/2026 8:29:56 PM. This article is licensed under a Creative Commons Attribution-NonCommercial 3.0 Unported Licence.

95 A. R. Sotiles and F. Wypych, *Inorg. Chem. Commun.*, 2023, **152**, 110698.

96 D. R. Anakha, K. M. Ashika and T. V. Vyshnavi, *et al.*, *RSC Appl. Interfaces*, 2025, **2**, 684–695.

97 A. Whitten, D. Guo, E. Tezel, R. Denecke, E. Nikolla and J.-S. McEwen, *JACS Au*, 2024, **4**, 3104–3117.

98 A. P. Dementjev, A. De Graaf, M. C. M. de Sanden, K. I. Maslakov, A. V. Naumkin and A. A. Serov, *Diam. Relat. Mater.*, 2000, **9**, 1904–1907.

99 S. Qin, L. Huang, Y. Zhang, T. Zhang, M. Tian and J. Jiang, *Sci. Rep.*, 2025, **15**, 787.

100 J. den Brand, P. C. Snijders, W. G. Sloof, H. Terryn and J. H. W. De Wit, *J. Phys. Chem. B*, 2004, **108**, 6017–6024.

101 L. Arjomandi-Behzad, Z. Alinejad, M. R. Zandragh, A. Golmohamadi and H. Vojoudi, *Iscience*, 2023, **26**, 106213.

102 P. M. Chamberlin and K. W. Adu, *MRS Adv.*, 2024, **9**, 1031–1036.

103 M. Long, D. Li, H. Li, X. Ma, Q. Zhao, Q. Wen and F. Song, *RSC Adv.*, 2022, **12**, 20946–20955.

104 A. Champati, P. K. Sahu, A. Rath, B. Naik and A. Pradhan, *ACS Omega*, 2025, **10**, 43871–43890.

105 R. Roto and G. Villemure, *J. Electroanal. Chem.*, 2002, **527**, 123–130.

106 B.-Y. Chang and S.-M. Park, *Annu. Rev. Anal. Chem.*, 2010, **3**, 207–229.

107 S. Nayak and K. M. Parida, *Sci. Rep.*, 2019, **9**, 2458.

108 Z. Wang, X. Song, Y. Liu, Z. Sun, X. Zhang, Y. Wang and S. Wang, *Nanomaterials*, 2025, **15**, 1255.

109 A. Sherryna, M. Tahir and Z. Y. Zakaria, *ACS Appl. Energy Mater.*, 2024, **7**, 6289–6311.

110 D. Wang, Z. Liu, Y. Hong, C. Lin, Q. Pan, L. Li and K. Shi, *RSC Adv.*, 2020, **10**, 34466–34473.

111 H. Wang, M. Li, Q. Lu, Y. Cen, Y. Zhang and S. Yao, *ACS Sustain. Chem. Eng.*, 2018, **7**, 625–631.

112 F. Tang, H. Bai, Y. Chen, C. Shi, D. Wang, Y. Zhang, W. Liu, L. Yang and L. Hu, *RSC Adv.*, 2024, **14**, 10056–10069.

113 Q. Ibrahim and S. Gharbia, *Int. J. Mol. Sci.*, 2024, **25**, 12730.

114 Q. Liu, X. Ji, J. Deng, H. Jiang, G. Li, Y. Ouyang, X. Li, C. Tang, X. Tan and X. Hu, *J. Environ. Chem. Eng.*, 2023, **11**, 110153.

115 J. Yang, J. Long, H. Huang, X. Yang and L. Wei, *Colloids Surfaces A Physicochem. Eng. Asp.*, 2023, **660**, 130846.

116 M. Yang and Y. Wang, *Langmuir*, 2024, **40**, 20368–20378.

117 P. Pang, H. Han, L. Hu, C. Guo, Y. Gao and Y. Xie, *J. Nat. Gas Sci. Eng.*, 2021, **94**, 104060.

118 S. Tharuman, R. Karthikeyani, S.-M. Chen, V. Balakumar, N. Nataraj and V. Sasirekha, *J. Environ. Chem. Eng.*, 2023, **11**, 111376.

119 P. Aggarwal, B. Singh and A. Paul, *Mater. Adv.*, 2023, **4**, 4377–4389.

120 M. Saeidi, M. A. Amidian, S. Sheybanikashani, H. Mahdavi, H. Alimohammadi, L. Syedmoradi, F. Mohandes, A. Zarrabi, E. Tamjid and K. Omidfar, *et al.*, *Biosensors*, 2022, **12**, 337.

121 H. Sheikhpoor, A. Saljooqi, T. Shamspur and A. Mostafavi, *Environ. Technol. Innov.*, 2021, **23**, 101649.

122 I. E. Khalil, P. Das, H. Küçükkeçeci, V. Dippold, J. Rabeah, W. Tahir, J. Roeser, J. Schmidt and A. Thomas, *Chem. Mater.*, 2024, **36**, 8330–8337.

123 J. Hu, G. Zhao, L. Wu, C. Sun, X. Long, X. Long and F. Jiao, *Ind. Eng. Chem. Res.*, 2022, **61**, 15225–15239.

124 R. D. C. Soltani, E. Abolhasani, M. Mashayekhi, N. Jorfi, G. Boczkaj and A. Khataee, *Chemosphere*, 2022, **303**, 135201.

125 X. Liu, Y. Zhou, S. Sun and S. Bao, *RSC Adv.*, 2023, **13**, 31528–31540.

126 Y. Jia, S. Jiang, Q. Ou, Y. Liu, J. Zhang, Y. Zhou, Y. Lian and H. Wang, *CrystEngComm*, 2024, **26**, 532–542.

127 Y. Yea, S. S. D. Elanchezhiyan, R. Saravanakumar, G. Jagan, J. U. Choi, K. Saravanakumar and C. M. Park, *Environ. Res.*, 2024, **247**, 118209.

128 G. Salehi, M. Bagherzadeh, R. Abazari, M. Hajilo and D. Taherinia, *ACS Omega*, 2024, **9**, 4581–4593.

129 C. Zhang, J. Wang, S. Liu, Y. Han, J. Wang and H. Wang, *J. Environ. Sci. Heal. Part B*, 2025, **60**, 79–90.

130 P. K. Sahu, A. Champati, A. Rath, S. Pradhan, A. Pradhan and B. Naik, *Nanoscale Adv.*, 2025, **7**, 5561–5579.

131 T. K. Pal, *Mater. Chem. Front.*, 2023, **7**, 405–441.

132 H. Sohrabi, S. Ghasemzadeh, Z. Ghoreishi, M. R. Majidi, Y. Yoon, N. Dizge and A. Khataee, *Mater. Chem. Phys.*, 2023, **299**, 127512.

133 V. Shukla, A. A. Kumar, N. Haq, S. Tothadi and K. A. Siddiqui, *CrystEngComm*, 2025, **27**, 3326–3344.

134 T.-Z. Xiong, M.-M. Wang, T.-L. Ren, J.-J. Hu, C. Cao and H.-R. Wen, *Dalton Trans.*, 2025, **54**, 6188–6194.

135 Y. Hidalgo-Rosa, Y. Echevarria-Valdés, M. Saavedra-Torres, D. Páez-Hernández, E. Schott and X. Zarate, *Dalton Trans.*, 2025, **54**, 6623–6636.

136 V. Shukla, A. A. Kumar, N. Haq and K. A. Siddiqui, *Mater. Res. Bull.*, 2025, 113539.

137 X.-Y. Guo, Z.-P. Dong, F. Zhao, Z.-L. Liu and Y.-Q. Wang, *New J. Chem.*, 2019, **43**, 2353–2361.

138 W. Li, X. Ma, S. Song, B. Shao, X. Liu and J. Chen, *New J. Chem.*, 2022, **46**, 22849–22861.

139 M. Kukreja, A. A. Kumar, N. Haq and K. A. Siddiqui, *Mater. Today Commun.*, 2025, **45**, 112403.

140 J. Li, L. Zou, J. Xu, Y. Wu, M. Afzal, A. Alarifi, D. Omoding, A. Kushwaha and A. Kumar, *J. Mol. Struct.*, 2025, **1321**, 140088.

141 V. Shukla, G. Aalam, S. W. Ali, A. A. Kumar, N. Haq and K. A. Siddiqui, *Appl. Organomet. Chem.*, 2025, **39**, e70339.

142 M. V. Varsha and G. Nageswaran, *Microchem. J.*, 2023, **188**, 108481.

143 S. Yang, K. Li, N. Sun, J. Liu, Q. Luo, Y. Zhang, L. Wang, S. Wu and M. Zhu, *Inorg. Chem. Commun.*, 2023, **158**, 111641.

144 V. Shukla, A. A. Kumar, N. Lee, D. Dewangan, R. Medishetty, M. Ahmad, N. Haq and K. A. Siddiqui, *Small*, 2025, e08916.

145 X. Fang, X. Chen, Y. Liu, Q. Li, Z. Zeng, T. Maiyalagan and S. Mao, *ACS Appl. Nano Mater.*, 2019, **2**, 2367–2376.

Open Access Article. Published on 08 April 2026. Downloaded on 4/8/2026 8:29:56 PM.
This article is licensed under a Creative Commons Attribution-NonCommercial 3.0 Unported Licence.

146 M. Yahyapour, M. Ranjbar and A. Mohadesi, *J. Mater. Sci.: Mater. Electron.*, 2021, **32**, 3180–3190.

147 J. Chuiprasert, S. Srinives, N. Boontanon, C. Polprasert, N. Ramungul, A. Karawek and S. K. Boontanon, *ACS Omega*, 2024, **9**, 23172–23183.

148 B. Wang and B. Yan, *Talanta*, 2020, **208**, 120438.

149 S. Meng, J. Liu, Y. Yang, S. Mao and Z. Li, *Sci. Total Environ*, 2024, **922**, 171115.

150 A. Rath, P. K. Sahu, A. Champati, A. Pradhan, A. Madhual, P. M. Mishra and B. Naik, *Discov. Appl. Sci.*, 2025, **7**, 1–23.

151 J. Wang, D. Zhi, H. Zhou, X. He and D. Zhang, *Water Res.*, 2018, **137**, 324–334.

152 X. Li, Q. Li, X. Chen, B. Yan, S. Li, H. Deng and H. Lu, *Nanomaterials*, 2025, **15**, 1108.

153 L. Li, J. Liu, J. Zeng, J. Li, Y. Liu, X. Sun, L. Xu and L. Li, *Nanomaterials*, 2021, **11**, 1660.

154 B. S. Subasi, T. Hayri-Senel, E. Kahraman, S. Sezer, G. Nasun-Saygili and N. Erdol-Aydin, *Sci. Rep.*, 2025, **15**, 25894.

155 F. Tamaddon, A. Nasiri and G. Yazdanpanah, *MethodsX*, 2020, **7**, 100764.